

On Energy Cascades in General Flows: A Lagrangian Application

Q Jamet, A Ajayi, J Le Sommer, T Penduff

Laboratoire de Glaciologie et Geophysique de l'Environnement, CNRS, Grenoble, France

A Hogg

Research School of Earth Sciences and ARC Centre of Excellence for Climate Extremes, Australian National University, Canberra, AU

WK Dewar*

Laboratoire de Glaciologie et Geophysique de l'Environnement, CNRS, Grenoble, France and Dept. of EOAS, Florida State University, Tallahassee, FL, 32306

Abstract

An important characteristic of geophysically turbulent flows is the transfer of energy between scales. Balanced flows pass energy from smaller to larger scales as part of the well-known upscale cascade while submesoscale and smaller scale flows can transfer energy eventually to smaller, dissipative scales. Much effort has been put into quantifying these transfers, but a complicating factor in realistic settings is that the underlying flows are often strongly spatially heterogeneous and anisotropic. Furthermore, the flows may be embedded in irregularly shaped domains that can be multiply connected. As a result, straightforward approaches like computing Fourier spatial spectra of nonlinear terms suffer from a number of conceptual issues. In this paper, we develop a method to compute cross-scale energy transfers in general settings, allowing for arbitrary flow structure, anisotropy and inhomogeneity. We employ a Green's function approach to the kinetic energy equation to relate kinetic energy at a point to its Lagrangian history. A spatial filtering of the resulting equation naturally decomposes kinetic energy into length scale dependent contributions and describes how the transfer of energy between those scales takes place. The method is applied to a doubly periodic simulation of vortex merger, resulting in the demonstration of the expected upscale energy cascade. Somewhat novel results are that the energy transfers are dominated by pressure work, rather than kinetic energy exchange, and dissipation is a noticeable influence on the larger scale energy budgets. We also describe, but do not employ here, a technique for developing filters to use in complex domains.

Keywords: energy transfers, energetics, balanced flow dynamics

1. Introduction

A surprising aspect of nonlinear geophysical flows; namely, that they transfer energy from smaller to larger scales and thus in a sense opposite to that of three-dimensional, isotropic turbulence, has been known for some time (Fjortoft (1953), Kraichnan (1967), Charney

This article has been accepted for publication and undergone full peer review but has not yet been through the copyediting, typesetting, pagination and proofreading process which may lead to differences between this version and the Version of Record. Please cite this article as doi: 10.1029/2020MS002900

September 9, 2020

Email address: wdewar@fsu.edu (WK Dewar) ©2020 American Geophysical Union. All rights reserved.

17 so-called ‘balanced’ dynamics, which strongly constrains vortex tube stretching. Scott and
18 Wang (2005) argue for the observation of an upscale cascade in the ocean from analysis of
19 satellite sea surface height measurements and Scott and Arbic (2007) argue for the same in
20 numerical models. Others have argued that this behavior in wavenumber space is accom-
21 panied by a transfer in the frequency domain to lower frequencies (Arbic et al. (2012)) and
22 extensions to the combined wavenumber frequency domain have also been found (Arbic et al.
23 (2014)).

24 An upscale cascade dynamically and importantly affects the ocean. For example, the
25 transfer from high frequency mesoscale variability to low frequencies implicates eddies as
26 a mechanism effecting climate variability (Holland (1978), Berloff and McWilliams (1999),
27 and Dijkstra and Molemaker (1999)). Further, the large scale circulation receives energy
28 from the large scale, slowly evolving winds (Wunsch and Ferrari (2004), Ferrari and Wunsch
29 (2009)) and it is generally thought this energy is shunted to the mesoscale by geostrophic
30 instabilities. An equilibrated ocean must then find a pathway for the mesoscale to lose its
31 energy, and the so-called upscale cascade presents a hindrance. The return of energy to
32 larger scales where dissipation is vanishingly weak has led to considerable recent interest in
33 mesoscale energy loss.

34 Given that cross scale energy exchange in the ocean is central to ocean and climate
35 dynamics, it is important to examine how those transfers can be measured. Most energy ex-
36 change diagnoses of both observations and models have proceeded through the use of Fourier
37 transforms (Arbic et al. (2014)), which requires that the data be converted into forms consis-
38 tent with the approach. Speaking primarily about spatial analyses, geographically confined
39 regions of interest are usually defined. Since the data are not spatially periodic, as assumed
40 by Fourier methods, tapering, or windowing, is usually applied. The subsequent analysis
41 then occurs on the windowed domain, and the results are in some sense representative of
42 an averaged statement of the transfers in the domain. Another complicating factor is that
43 irregularities can appear inside the domain. An example is Bermuda, sitting in the open
44 Atlantic at a location near to the Gulf Stream and the separated North Atlantic jet. Meth-
45 ods, often subjective, are required to handle such areas, frequently involving an interpolation
46 over the problematic regions. Nonetheless, these analyses have usually yielded answers con-
47 sistent with our theoretical expectations. They do represent spatial averages however, and
48 further understanding of inhomogeneous regions, like the Kuroshio and the Gulf Stream,
49 require more spatial resolution. This served in part as motivation for Aluie et al. (2018) who
50 examined energy exchanges locally based on a purely spatial filtering approach.

51 The focus of this paper is to propose a new method for analyzing kinetic energy in models
52 and observations that appears to avoid many of the above mentioned issues with Fourier
53 methods. It also differs from previous approaches in several ways, primarily in focussing on
54 a Lagrangian-like approach and working directly with the kinetic energy equation. We apply
55 the technique to primitive equation model output describing vortex merger, and hence an
56 upscale cascade. The results indicate an upscale cascade, thus demonstrating the viability of
57 the procedure, even though it is not limited to this restrictive setting. The theoretical basis
58 for the procedure is outlined in the next section, the model description and applications
59 appear in the following section. We discuss and summarize the paper in the concluding
60 section, emphasizing new results specific to the energetics of the upscale cascade and outline
61 thoughts for further work. Methods to handle domain irregularities are outlined in Appendix

62 A. An Eulerian version of the present analysis appears in Appendix B. Derivation of
 63 comparable formulas for potential energy are discussed in Appendix C and modifications to
 64 the analysis introduced when using isopycnal coordinates are outlined in Appendix D.

65 2. An Analysis of the Kinetic Energy Equation

66 2.1. Overview

67 Below we present an analysis of the kinetic energy equation. In brief, our plan is to
 68 apply a Green's function analysis to the kinetic energy equation. The result relates the
 69 final kinetic energy of a parcel to its initial kinetic energy and its history along its (quasi-)
 70 Lagrangian trajectory. We then filter this equation in physical space to obtain a statement
 71 about a length scale based decomposition of the final kinetic energy. Similar filterings of
 72 the initial kinetic energy and kinetic energy sources then yield statements about cross-scale
 73 energy transfers. Finally, we average the point-wise kinetic energy decomposition to obtain a
 74 more representative view of the cross-scale transfers. These steps are spelled out in sequence
 75 in the following subsections. The reader wishing to skip mathematical detail can go directly
 76 to equations (36) - (38), where the results are summarized.

77 We begin with the hydrostatic equations in Cartesian coordinates, the zonal momentum
 78 component of which is

$$u_t + uu_x + vu_y + wu_z - fv = -p_x + \nu(u_{xx} + u_{yy} + u_{zz}) \quad (1)$$

79 where u is zonal velocity, subscripts x , y , z , and t denote partial derivatives with respect to
 80 zonal, meridional and vertical location and time, respectively. The quantity p is pressure and
 81 ν is viscosity. A partial step to constructing the kinetic energy equation involves multiplying
 82 (1) by u , which results in

$$(u^2/2)_t + u(u^2/2)_x + v(u^2/2)_y + w(u^2/2)_z - fuv = \\ -up_x + (\nu(uu_x))_x + (\nu(uu_y))_y + (\nu(uu_z))_z - \nu(u_x)^2 - \nu(u_y)^2 - \nu(u_z)^2 \quad (2)$$

83 A similar procedure on the meridional momentum equation and adding returns the kinetic
 84 energy equation

$$K_t + \nabla \cdot \mathbf{u}K = -\mathbf{u}_h \cdot \nabla_h p - \epsilon + \nabla \cdot (\nu \nabla K) \quad (3)$$

85 where $K = u^2/2 + v^2/2 = |\mathbf{u}_h|^2/2$ and $\epsilon = \nu \nabla \mathbf{u}_h \cdot \nabla \mathbf{u}_h = \nu |\nabla \mathbf{u}_h|^2$ is dissipation. We rewrite
 86 this as

$$K_t + \nabla \cdot \mathbf{u}K - \nabla \cdot (\nu \nabla K) = R \quad (4)$$

87 where $R = -\mathbf{u}_h \cdot \nabla_h p - \epsilon$ contains the ‘sources’ and ‘sinks’ for kinetic energy. Given that
 88 pressure gradients appear in the momentum equations as a force acting on a fluid particle,
 89 the quantity $-\mathbf{u}_h \cdot \nabla_h p$ represents movement in the direction of a force. We will thus refer
 90 to it as ‘pressure work’. The quantity $-\epsilon$ is simply dissipation of kinetic energy.

91 Exploiting the hydrostatic balance, pressure work can be rewritten as

$$-\mathbf{u}_h \cdot \nabla_h p = -\nabla \cdot \mathbf{u}p + wb \quad (5)$$

92 where b is buoyancy. The last quantity in (5) is the exchange between kinetic and potential
 93 energy. In this paper we work primarily with pressure work, noting that potential energy
 94 exchange is a component of pressure work.

95 2.2. Comparison to Other Approaches

96 Working directly with kinetic energy, via (4), distinguishes this approach from others.
97 Traditional Fourier analysis proceeds by transforming (1) and multiplying by the momentum
98 transform conjugate $\hat{u}(\mathbf{k})^*$ where \mathbf{k} denotes a wavenumber. The result ($\hat{E}(\mathbf{k}) = (\hat{u}\hat{u}^* + \hat{v}\hat{v}^*)/2$)
99 is usually interpreted as the energy spectrum although more properly it is related to the
100 momentum spectrum. The relation of $\hat{E}(\mathbf{k})$ to energy comes indirectly from Parseval's
101 equality, i.e.

$$\int_V K dx = \int_{\mathbf{k}} E(\mathbf{k}) d\mathbf{k} \quad (6)$$

102 which, while useful, argues this approach is restricted to integral statements. In contrast,
103 the Fourier transform of K is

$$\hat{K}(\mathbf{k}) = \frac{1}{2} \int_{\mathbf{p}} [\hat{u}(\mathbf{p})\hat{u}(\mathbf{k} - \mathbf{p}) + \hat{v}(\mathbf{p})\hat{v}(\mathbf{k} - \mathbf{p})] d\mathbf{p} \quad (7)$$

104 which, although quite different from $\hat{E}(\mathbf{k})$, still satisfies Parseval's identity while being di-
105 rectly related to kinetic energy.

106 To probe into the spatial structure of energy transfers, it is natural to remain in the
107 physical domain. In this sense, our approach is like that of Aluie et al. (2018). We differ
108 from them in that they 'coarse-grain' (1) and multiply by the coarse grained velocity to
109 obtain an equation describing $\bar{K} = 0.5(\bar{u}^2 + \bar{v}^2)$, where the bar denotes the coarsening
110 operator. In the process, terms appear in the \bar{K} equation involving third order quantities
111 like $\bar{u}(\bar{u}\bar{u}_x) - \bar{u}(\bar{u}\bar{u}_x)$, which in the LES community are interpreted as measuring the energy
112 cascade due to wave-mean flow interaction. They describe the effect on \bar{K} , following a parcel
113 moving at \bar{u} , of 'sub-grid' scale processes.

114 Clearly the coarsening operator is one of the primary distinctions between Aluie et al.
115 (2018) and the present approach. In fact, if we choose the coarsening operator as a Dirac delta
116 function, then $\bar{u} = u$ and our approaches merge. The cost of this choice is the wave-mean
117 flow interaction term vanishes, leading to the statement that the unfiltered equations do not
118 cascade. In our view, cascading is broader than wave-mean flow interaction and occurs in
119 unfiltered results, as evidenced in Fig. 1. The panels show results from the numerical model
120 discussed in detail later in the paper. For now, we mention they are plots of kinetic energy in
121 a layer and come from day 20 and day 585 of a doubly periodic numerical experiment typified
122 by vortex merger. Both plots are in physical space and neither plot has been coarse-grained
123 or filtered. Visual comparison suggests the later plot is characterized by larger length scales
124 than the earlier. Spectra of 'normalized' kinetic energy, i.e. of the variable $\kappa = a(t)K$, for
125 both days, taken along the line in Fig. 1 (right), appear in Fig. 2. The integrated kinetic
126 energies along this line were used to normalize the kinetic energies, i.e. $a(t) = (\int_y K(t) dy)^{-1}$,
127 so that the total integral in both plots, $\int_y \kappa dy$, was unity. This was done to remove amplitude
128 variations that would interfere with the comparisons of the wavenumber content. The earlier
129 spectrum (red) is characterized by enhanced energies at higher wavenumbers, while the later
130 (blue) shows elevated levels at lower wavenumbers. Clearly a 'cascade' has occurred in these
131 unfiltered plots and it is this behavior we seek to quantify.

132 Although our procedure differs from that of Aluie et al. (2018), we do not criticize their
133 approach. They adopt a procedure of clear relevance to modelers interested in parameteri-
134 zation. Our approach is meant for the full diagnosis of 'eddy-resolving' models.

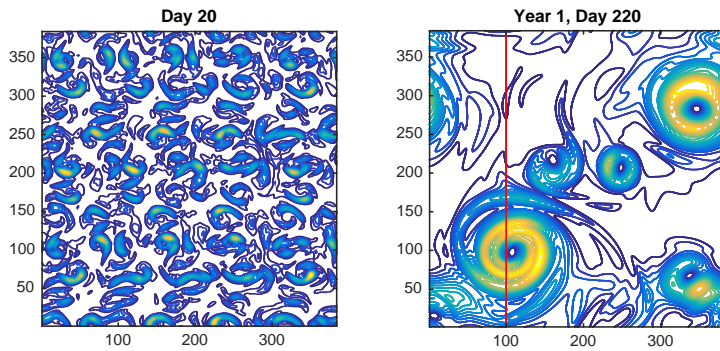


Figure 1: Distribution of kinetic energy in layer two of our 4 layer model on (left) year 0 day 20 and year 1 day 220 (right)

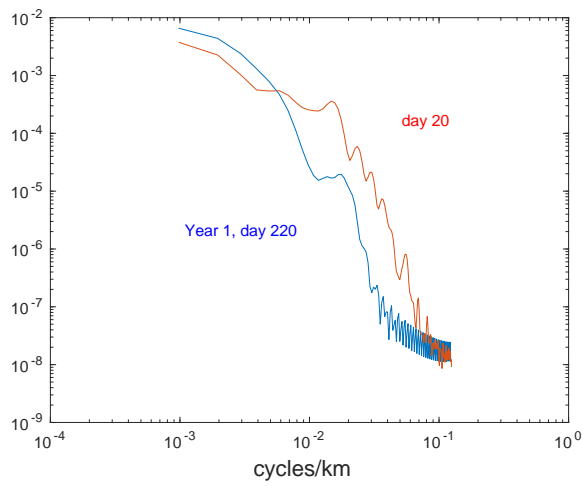


Figure 2: Spectra of kinetic energy \hat{K} from year 0 day 20 (red) and year 1 day 220 (blue). Clearly a cascade of kinetic energy to larger scales has occurred in this unfiltered view of kinetic energy.

¹³⁵ 2.3. *Kinetic Energy at a Single Point*

¹³⁶ We now apply a Green's function analysis, which leads eventually to the construction
¹³⁷ of kinetic energy at a point, and begins by multiplying (4) by some space-time dependent
¹³⁸ function G .

$$GK_t + G\nabla \cdot \mathbf{u}K - G\nabla \cdot (\nu \nabla K) = GR \quad (8)$$

¹³⁹ Straightforward calculus leads to

$$\begin{aligned} (GK)_t + \nabla \cdot \mathbf{u}GK - \nabla \cdot (\nu G \nabla K) + \nabla \cdot (K \nu \nabla G) \\ - K(G_t + \nabla \cdot \mathbf{u}G + \nabla \cdot (\nu \nabla G)) = RG \end{aligned} \quad (9)$$

¹⁴⁰ Again, appealing to straightforward Green's function methods, we suppose G satisfies

$$G_t + \nabla \cdot \mathbf{u}G = -\nabla \cdot (\hat{\nu} \nabla G) - \delta(\mathbf{x} - \mathbf{x}_o, t - t_o) \quad (10)$$

141 where δ is the usual Dirac delta function centered on the so-called ‘source points’ \mathbf{x}_o, t_o and
 142 $\hat{\nu}$ is a viscosity-like quantity. It is not necessarily equal to ν , although in this paper we will
 143 always discuss cases where $\hat{\nu} = \nu$. Boundary conditions are required to solve (10). As is
 144 typical for Green’s functions, the boundary conditions will always be homogeneous, however
 145 how they will be distributed between specified values of G and its normal derivatives on the
 146 boundary are yet to be determined.

147 Eq. (10) is almost a simple advection-diffusion equation, differing only because viscosity
 148 appears multiplied by -1 , i.e. $-\hat{\nu} < 0$, as opposed to $\hat{\nu} > 0$ occurs on the right hand
 149 side. In fact, such a result is standard in Green’s function analyses, where the equation
 150 solved by G is the adjoint of the equation governing K , and is handled by solving (10)
 151 backwards in time. Instead of an initial condition, a ‘posterior’ condition on G is applied,
 152 and integration proceeds to temporally earlier values. For this case, we will always choose a
 153 posterior condition of $G(t_f) = 0$. Notationally, $G = G(\mathbf{x}, t; \mathbf{x}_o, t_o)$, expressing the dependence
 154 of G on both the ‘source’ points, \mathbf{x}_o, t_o , and the ‘observation’ points, \mathbf{x}, t .

155 Now, we perform an integral of (9) over a volume V of the observation space, \mathbf{x} , and over
 156 the time interval 0 to t_o , where $0 < t_o$.

$$K(\mathbf{x}_o, t_o) - \int_{\mathbf{x}} GK(\mathbf{x}, 0)d\mathbf{x} + \int_0^{t_o} \int_S (\underline{u}GK - \hat{\nu}G\nabla K + \hat{\nu}K\nabla G) \cdot \vec{n}dSdt = \quad (11)$$

$$\int_0^{t_o} \int_{\mathbf{x}} RGd\mathbf{x}dt + \int_0^{t_o} \int_{\mathbf{x}} G\nabla \cdot ((\nu - \hat{\nu})\nabla K)d\mathbf{x}dt$$

157 where S is the surface bounding the volume V . At this point, we exploit the available
 158 flexibility in boundary conditions. Eq. (11) describes how various kinetic energy sources
 159 contribute to the final kinetic energy at a point. From a physical perspective, we expect
 160 kinetic energy transport across the boundary S can contribute to the final kinetic energy
 161 inside S . This can occur by kinetic energy advection and viscous exchange across S . Both
 162 of these appear in (11) multiplied by G . We therefore choose to apply $\nabla G \cdot \vec{n} = 0$, i.e.
 163 homogenous Neumann boundary conditions, to G , thus eliminating the underlined term
 164 from (11) and preserving the aforementioned physical effects.

165 Suppose first V is a closed domain. With this, and a rearrangement of terms, we obtain

$$K(\mathbf{x}_o, t_o) = \int_{\mathbf{x}} G(\mathbf{x}, 0; \mathbf{x}_o, t_o)K(\mathbf{x}, 0)d\mathbf{x} + \int_0^{t_o} \int_{\mathbf{x}} \hat{R}Gd\mathbf{x}dt \quad (12)$$

166 where

$$\hat{R} = R + \nabla \cdot ((\nu - \hat{\nu})\nabla K)$$

167 as the boundary fluxes all vanish.

168 Eq. (12) illustrates how the kinetic energy at location \mathbf{x}_o and time t_o has been con-
 169 structed. The first term on the right hand side represents the ‘initial’ kinetic energy, $K(\mathbf{x}, 0)$
 170 that ends up at (\mathbf{x}_o, t_o) . The volume defining the impact of this $K(\mathbf{x}, 0)$ contribution de-
 171 pends on the development of G from t_o . The last term involves the internal fluid sources
 172 of kinetic energy and how they have contributed to K along the trajectory that eventually
 173 ends up at \mathbf{x}_o . Eq. (12) provides a full deconstruction of the kinetic energy in the basin,
 174 regardless of spatial inhomogeneities in the flow.

If V is an open domain or a subdomain of a full, closed basin, (12) is augmented by advective and diffusive fluxes of kinetic energy across the subdomain boundary, to the extent they are involved as measured by G . These vanish identically in the presence of doubly-periodic conditions, which will describe our application in this manuscript. But even for the most general case, boundary contributions can be made small by choosing a domain large enough that advection and diffusion do not have time to reach the boundaries. We will proceed here ignoring boundary contributions.

The clearest interpretation of this formula occurs if G , defined in (10), measures purely Lagrangian trajectories, which occurs in the limit $\hat{\nu} = 0$. For the remainder of this paper, we will continue with $\hat{\nu} = \nu$ both for simplicity and because our numerical application will employ a very small value for ν . We have also checked that our results are insensitive to $\hat{\nu} < \nu$. It is in the nearly Lagrangian nature of (12) that the present approach somewhat resembles that of Nagai et al. (2015) and Shakespeare and Hogg (2017). K. Srinivasan has also alerted us to early contributions by Kraichnan (Kraichnan (1964); Kraichnan (1967)) in which a Green's function based analysis of turbulence was employed. There are similarities in our approaches but the objectives our studies differ. Kelley et al. (2013) also explored the coarse graining decomposition in Aluie et al. (2018) in a Lagrangian setting with a focus on Lagrangian Coherent Structures.

2.4. Cross-scale Contributions to Kinetic Energy

We now compute how energy is transferred between various length scales. These exchanges become more complicated when $K(\mathbf{x}_o, t_o)$ is strongly inhomogeneous and anisotropic, as is typical in the ocean. In this and the next subsections, we will build to a formal statement of cross-scale transfers in several steps, proceeding from a statement valid at a single point to one averaged over a specified volume.

As a first step, consider a ‘filter’ applied to $K(\mathbf{x}_o, t_o)$, i.e.

$$K_L(\mathbf{x}_1, t_o) = \int_{\mathbf{x}_o} K(\mathbf{x}_o, t_o) f_L(\mathbf{x}_o - \mathbf{x}_1) d\mathbf{x}_o \quad (13)$$

where f_L is a filter associated with a length scale, L , and fixed at location \mathbf{x}_1 . What the filter might be is a question deserving discussion, because the filtering will be carried out in physical space. For realistic problems, physical space typically contains a lot of irregularity: examples are complex lateral boundaries and major topography that can extend through domains at given depths and reach up to the surface. Any useful filter must contend with these features. Guidance about the filters can be obtained from the simplest case of an unbounded domain without interior obstacles. In that case, as we argue below, the obvious choices are trigonometric functions. At a more fundamental level, these work because they are a collection of functions forming a complete set due to their being the eigenfunction, eigenvalue solutions to the Helmholtz equation in an unbounded domain. We argue in Appendix A basis functions constructed from the Helmholtz equation with homogeneous conditions on S , the boundary of the domain V , will for complex domains provide a collection of functions with the desired properties. We stress here, however, that Appendix A is not exploited in the present paper, but serves as a procedure in need of further examination.

²¹⁴ But whatever the filter is, an important point is that the filter works on the ‘source
²¹⁵ points’ (\mathbf{x}_o) of the Green’s function. Operating on (12), we obtain

$$K_L(\mathbf{x}_1, t_o) = \int_{\mathbf{x}} G_L K(\mathbf{x}, 0) d\mathbf{x} + \int_o^{t_o} \int_{\mathbf{x}} R G_L d\mathbf{x} dt \quad (14)$$

²¹⁶ where

$$G_L(\mathbf{x}, t; \mathbf{x}_1, t_o) = \int_{\mathbf{x}_o} G(\mathbf{x}, t; \mathbf{x}_o, t_o) f_L(\mathbf{x}_o - \mathbf{x}_1) d\mathbf{x}_o \quad (15)$$

²¹⁷ We can similarly filter (10) to show

$$\frac{\partial}{\partial t} G_L + \nabla \cdot \mathbf{u} G_L = -\nabla(\nu \cdot \nabla G_L) - f_L(\mathbf{x} - \mathbf{x}_1) \delta(t - t_o) \quad (16)$$

²¹⁸ We want the filtering to decompose $K(\mathbf{x}_1, t_o)$ completely into scale dependent information,
²¹⁹ i.e.

$$\int_{L=0}^{\infty} K_L(\mathbf{x}_1, t_o) dL = K(\mathbf{x}_1, t_o) \quad (17)$$

²²⁰ Employing (13) in (17), it is simple to show

$$\int_{L=0}^{\infty} f_L(\mathbf{x}_o - \mathbf{x}_1) dL = \delta(\mathbf{x}_o - \mathbf{x}_1) \quad (18)$$

²²¹ where δ is the Dirac delta function¹. A classic result from the theory of generalized functions
²²² is

$$\int_{-\infty}^{\infty} e^{-2\pi \mathbf{k} \cdot (\mathbf{x}_o - \mathbf{x}_1)} d\mathbf{k} = \Pi_{i=1}^3 \int_{-\infty}^{\infty} e^{-2\pi k_i (x_{i,o} - x_{i,1})} dk_i = \delta(\mathbf{x}_o - \mathbf{x}_1) \quad (19)$$

²²³ where the index i denotes dimensions and Π implies multiplication. Working now with one
²²⁴ of the dimensions, suppressing the subscript i , breaking the integral into real and imaginary
²²⁵ parts and using symmetry implies

$$2 \int_o^{\infty} \cos(2\pi k(x_o - x_1)) dk = \delta(x_o - x_1) \quad (20)$$

²²⁶ Last, we employ the relation between wavenumber and wavelength, $k = 1/L$, to obtain

$$2 \int_o^{\infty} \frac{\cos(2\pi(x_o - x_1)/L)}{L^2} dL = \delta(x_o - x_1) \quad (21)$$

²²⁷ which effectively defines our original filter, f_L , for a single spatial dimension

$$f_L(x_o - x_1) = 2 \frac{\cos(\frac{2\pi(x_o - x_1)}{L})}{L^2} \quad (22)$$

²²⁸ To filter over a group of length scales L_x , L_y , L_z in three dimensions, one employs the
²²⁹ product of (22) appropriate to each dimension. The quantity $K_L(\mathbf{x}_1, t_o)$ represents the
²³⁰ energy resident in $K(\mathbf{x}_1, t_o)$ between the length scales L and $L + \delta L$.

¹This property of the basis set is essential to their role in filtering. We will revisit it in Appendix A when developing more general basis sets.

231 2.5. Band Pass Filtering of Final Kinetic Energy

232 The second step in formulating cross-scale transfers is to represent the energy at \mathbf{x}_1
 233 resident between scales of L_j and L_k by suitable integration over length scales. For example,
 234 the energy at scales L_j and greater becomes (again working in one dimension)

$$\begin{aligned}\kappa_{L_j}^{\infty}(\mathbf{x}_1, t_o) &= \int_{L_j}^{\infty} K_L(\mathbf{x}_1, t_o) dL \\ &= \frac{2}{L_j} \int_{-\infty}^{\infty} \text{sinc}(2\pi \frac{(x_o - x_1)}{L_j}) K(\mathbf{x}_o, t_o) d\mathbf{x}_o\end{aligned}\quad (23)$$

235 where

$$\text{sinc}(x) = \frac{\sin(x)}{x} \quad (24)$$

236 is the well known ‘sinc’ function, often found in signal detection applications. The remainder
 237 of the energy at shorter lengths is

$$\kappa_o^{L_j} = K(\mathbf{x}_1, t_o) - \kappa_{L_j}^{\infty}(\mathbf{x}_1, t_o) \quad (25)$$

238 Analogous to (15), we define

$$\Gamma_{L_j}^{L_k}(\mathbf{x}, t; \mathbf{x}_1, t_o) = \int_{\mathbf{x}_o} \int_{L_j}^{L_k} f_L(\mathbf{x}_o - \mathbf{x}_1) dL G(\mathbf{x}, t; \mathbf{x}_o, t_o) d\mathbf{x}_o \quad (26)$$

239 and find that it is governed by

$$\frac{\partial}{\partial t} \Gamma_{L_j}^{L_k} + \nabla \cdot \mathbf{u} \Gamma_{L_j}^{L_k} = -\nabla \cdot (\nu \nabla \Gamma_{L_j}^{L_k}) - \gamma_{L_j}^{L_k}(\mathbf{x}_1 - \mathbf{x}) \delta(t - t_o) \quad (27)$$

240 where

$$\gamma_{L_j}^{L_k}(\mathbf{x}_1 - \mathbf{x}) = \int_{L_j}^{L_k} f_L(\mathbf{x}_1 - \mathbf{x}_o) dL \quad (28)$$

241 This more general formulation anticipates that the length scale dependent basis functions
 242 needed to probe the scale dependent structure of K in general domains will not typically be
 243 trigonometric functions. See the Appendix A for more discussion. We will frequently refer
 244 to $\gamma_{L_j}^{L_k}$ in the following as a ‘filter’.

245 The construction of the kinetic energy at \mathbf{x}_1 between L_j and L_k can be written

$$\kappa_{L_j}^{L_k}(\mathbf{x}_1, t_o) = \int_{\mathbf{x}} \Gamma_{L_j}^{L_k} K(\mathbf{x}, 0) d\mathbf{x} + \int_o^{t_o} \int_{\mathbf{x}} R(\mathbf{x}, t) \Gamma_{L_j}^{L_k} d\mathbf{x} dt$$

246 where

$$\kappa_{L_j}^{L_k}(\mathbf{x}_1, t_o) = \int_{L_j}^{L_k} K_L(\mathbf{x}_1, t_o) dL = \int_{L_j}^{L_k} \int_{\mathbf{x}} K(\mathbf{x}, t_o) f_L(\mathbf{x} - \mathbf{x}_1) d\mathbf{x} dL \quad (29)$$

247 Note that (29) is a Lagrangian statement of kinetic energy exchange, in that the modified
 248 Green’s function $\Gamma_{L_j}^{L_k}$ tracks fluid movements between the final time $t = t_o$ and the initial
 249 time $t = 0$. It is also possible to use this formalism to render an Eulerian statement about
 250 kinetic energy exchange. This is discussed in Appendix B. We continue here with the
 251 Lagrangian formalism, such having been less discussed in the literature (but see Kelley et al.
 252 (2013)).

253 *2.6. Band Pass Filtering of Kinetic Energy Sources*

254 The third step addresses the cross scale exchanges involved in the creation of $\kappa_{L_j}^{L_k}$. Consider
 255 the ‘initial’ kinetic energy, appearing as the first term on the right hand side of (29).
 256 Exploiting (18), this quantity can be rewritten

$$K(\mathbf{x}, 0) = \int_{\lambda} K_{\lambda}(\mathbf{x}, 0) d\lambda = \sum_{i=0}^N \kappa_{L_i}^{L_{i+1}}(\mathbf{x}, 0) \quad (30)$$

257 where the interval $L = 0$ to $L = \infty$ has been broken into $N + 1$ separate intervals and,
 258 equating L_j to L_i and L_k to L_{i+1} , $\kappa_{L_i}^{L_{i+1}}$ is as in (29). Rearranging yields

$$\begin{aligned} & \int_{\mathbf{x}} \Gamma_{L_j}^{L_k}(\mathbf{x}, 0; \mathbf{x}_1, t_o) K(\mathbf{x}, 0) d\mathbf{x} = \\ & \sum_{i=0}^N \int_{\mathbf{x}} \Gamma_{L_j}^{L_k}(\mathbf{x}, 0; \mathbf{x}_1, t_o) \kappa_{L_i}^{L_{i+1}}(\mathbf{x}, 0) d\mathbf{x} \end{aligned} \quad (31)$$

259 Eq. (31) expresses how the scale dependent decomposition of the initial kinetic energy
 260 contributes to the kinetic energy between L_j and L_k found in the final state. To the extent
 261 that the quantity

$$K_{L_j, L_i}^{L_k, L_{i+1}}(\mathbf{x}_1, 0) = \int_{\mathbf{x}} \Gamma_{L_j}^{L_k}(\mathbf{x}, 0; \mathbf{x}_1, t_o) \kappa_{L_i}^{L_{i+1}}(\mathbf{x}, 0) d\mathbf{x} \quad (32)$$

262 does not vanish for L_i, L_{i+1} outside the range L_j to L_k , there has been cross-scale transfer
 263 of kinetic energy. This calculation can be repeated for each band L_i to L_{i+1} to obtain a
 264 complete breakdown of the cross-scale transfers from the initial data to the final. Further,
 265 this computation can be performed for any time between the initial and final times, thus
 266 providing a time series of cross-scale kinetic energy exchanges. Similar decompositions into
 267 scale dependent contributions can be formed from the boundary terms and the source terms
 268 in R .

269 These lead to a complete reconstruction of the kinetic energy at any given scale from
 270 large and small scale structures occurring along the quasi-Lagrangian fluid path which, in
 271 turn, are measures of energy transfers across scales. Examining the time series of these
 272 terms identifies critical points in time when transfers are at their greatest. This information,
 273 along with knowledge of the spatial Green’s functions structures at those times, identifies
 274 the particular events associated with the transfers. A relatively complete overall picture of
 275 the energetics of the fluid can be developed.

276 *2.7. Area Averaging*

277 At this point, cross-scale transfers have been formally identified, with perhaps the strongest
 278 restriction being that they apply to the development of kinetic energy at a given point. How-
 279 ever, it might prove useful to have such a statement averaged over a given area. For example,
 280 for the case of merging vortices, one might be interested in an averaged statement of the
 281 construction of the energy averaged over the area of the merged vortex. We will pursue this
 282 goal in the next section. For now, we note that this once again reduces to an operation
 283 on the source points of the Green’s functions and can be obtained following the procedures
 284 described above.

285 Suppose that we want a simple ‘top-hat’ averaging of the results over a given domain,
 286 such as would be obtained according to

$$\overline{\kappa_{L_j}^{L_k}}(\boldsymbol{\xi}, t_o) = \int_{\mathbf{x}} \Pi_Q(\mathbf{x}_1 - \boldsymbol{\xi}) \kappa_{L_j}^{L_k}(\mathbf{x}_1, t_o) d\mathbf{x}_1 \quad (33)$$

287 where Π_Q is the top-hat function defined by

$$\Pi_Q(\mathbf{x}) = \frac{1}{Q^2} \quad (\mathbf{x} \in A) \quad (34)$$

$$= 0 \quad otherwise \quad (35)$$

288 with A a square centered on $\mathbf{x} = 0$ of area Q^2 . Following the steps outlined previously leads
 289 to

$$\begin{aligned} \overline{\kappa_{L_j}^{L_k}}(\boldsymbol{\xi}, t_o) &= \sum_{n=o}^N \int_{\mathbf{x}} \Phi_{L_j}^{L_k}(\mathbf{x}, 0; \boldsymbol{\xi}, t_o) \kappa_{L_n}^{L_{n+1}}(\mathbf{x}, 0) d\mathbf{x} \\ &\quad + \sum_{n=o}^N \int_o^{t_o} \int_{\mathbf{x}} \Phi_{L_j}^{L_k}(\mathbf{x} - \boldsymbol{\xi}, t) \rho_{L_n}^{L_{n+1}}(\mathbf{x}, t) d\mathbf{x} dt \end{aligned} \quad (36)$$

290 where $\rho_{L_n}^{L_{n+1}}$ is the analog to (29) for the energy source terms and we have assumed the
 291 boundary contributions vanish. The quantity $\Phi_{L_j}^{L_k}$ is governed by

$$\frac{\partial}{\partial t} \Phi_{L_j}^{L_k}(\mathbf{x}, t; \boldsymbol{\xi}, t_o) + \nabla \cdot \mathbf{u} \Phi_{L_j}^{L_k} + \nabla \cdot (\nu \nabla \Phi_{L_j}^{L_k}) = -\pi_{Q, L_j}^{L_k}(\mathbf{x} - \boldsymbol{\xi}) \delta(t - t_o) \quad (37)$$

292 where

$$\pi_{Q, L_j}^{L_k}(\mathbf{x} - \boldsymbol{\xi}) = \int_{\mathbf{x}_1} \Pi_Q(\mathbf{x}_1 - \boldsymbol{\xi}) \gamma_{L_j}^{L_k}(\mathbf{x}_1 - \mathbf{x}) d\mathbf{x}_1 \quad (38)$$

293 We will mostly work with the ‘modified’ Green’s function $\Phi_{L_j}^{L_k}$ in this paper and will call
 294 $\pi_{Q, L_j}^{L_k}$ a sampling function.

295 Although not pursued here, a similar approach can be applied to the potential energy
 296 equation. The details appear in Appendix C. Recall kinetic energy connects to potential
 297 energy through pressure work.

298 To summarize, (36) equates the scale dependent content of the kinetic energy between
 299 lengths L_j and L_k , averaged over the A (see (34)), to contributions from the initial kinetic
 300 energy, pressure work and dissipation.

301 3. Application to Merging Vortices

302 We now apply the previous methodology to a classical GFD problem; namely, the merger
 303 of like-signed vortices. We choose this as a first test case because this scenario is usually
 304 identified with the upscale cascade of rotating flows. In this sense, we know what the answer
 305 should be, broadly speaking, and so can judge the utility of the procedure. In addition, we
 306 can examine what new information is provided by this approach.

307 For this purpose, we used the recently developed MOM6 model². This model includes
 308 a number of modern features: most importantly it can be deployed in a purely isopycnal

²<https://github.com/NOAA-GFDL/MOM6>

309 configuration. There are relatively minor modifications to the kinetic energy equation in this
 310 setting, all of which are detailed in Appendix D. Perhaps the most significant details are
 311 that the Green's function equation is modified by the appearance of layer thickness in the
 312 viscous term, and the velocity field must be treated as compressible.

313 Our model consisted of a four layer f -plane fluid, with three subsurface interfaces, in a
 314 flat bottomed basin of 4000m total depth. The free surface and third layer interface were
 315 initially taken as flat, and the second layer, bounded by the first and second interfaces, was
 316 seeded with an organized distribution of 200m thick anomalies. All initial velocities were
 317 assumed to vanish. As expected, after a very short time adjustment involving gravity wave
 318 radiation, the fluid followed a classical path of like-signed vortex merger and opposite signed
 319 vortex propagation towards a final state of a single cyclonic-anticyclonic pair. Along the
 320 way, smaller vortices are swallowed by larger ones and a recognizable upscale energy cascade
 321 takes place. Examples of the fluid state at days 50, 135 and 220 in year 2 of the simulation
 322 appear in Fig. 3 in which this sequence is evident.

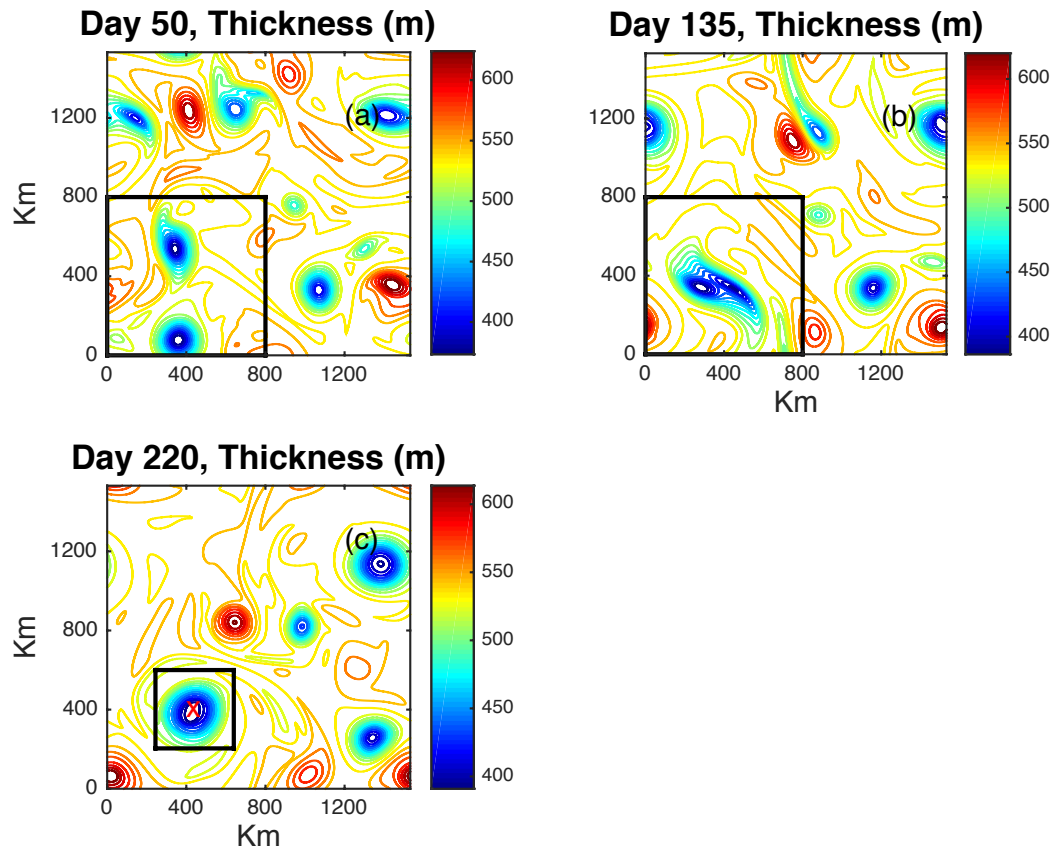


Figure 3: Three separate model states from a simulation of the MOM6 model with merging vortices. The top panels are of second layer thickness at days 50 (left) and 135 (right) and the bottom row shows day 220. The quadrant enclosed by the heavy black lines in the upper panels contains two cyclonic vortices in the process of merger. The smaller square centered on the red 'X' at day 220 encloses the merged vortex and indicates the region over which the analysis takes place.

323 Numerical details of the simulation appear in Table 1; here we emphasize that the result-
 324 ing internal deformation radii, 34km , 19km and 14km , are representative of the open ocean.
 325 The experiment was simulation for a total of four years, from which we focus on the analysis
 326 of days 50 to 220 from the second year of the simulation. The sequence in Fig. 3 comes
 327 from that interval, and we have focussed our attention on the merger event occurring in the
 328 lower, left hand quadrant outlined by the black lines in the upper two panels. Qualitatively,
 329 the two vortices near the bottom of panel (a) on day 50, with radial length scales of roughly
 330 100km , merge into the single, larger vortex seen in panel (c) at day 220. The smaller square
 331 in panel (c) encloses the region over which averaging takes place (see (33)).

Quantity	Parameter	Value
zonal grid scale	dx	4000m
meridional grid scale	dy	4000m
time step	dt	300s
zonal grid points	nx	384
meridional grid points	ny	384
Coriolis parameter	f	10^{-4}s^{-1}
gravity	g	9.8m/s^2
layer 1 density	ρ_1	1025kg/m^3
layer 2 density	ρ_2	1026.5kg/m^3
layer 3 density	ρ_3	1027.5kg/m^3
layer 4 density	ρ_4	1028kg/m^3
total depth	H	4000m
lateral viscosity	ν	$40\text{m}^2/\text{s}$

Table 1: Numerical parameters and values.

332 Closing budgets as we are attempting to do here requires high accuracy, especially in
 333 the solution of the adjoint equation. MOM6 does not have an adjoint option, so the fol-
 334 lowing procedure was adopted. Output from the merger experiment of horizontal velocity
 335 components and thickness were catalogued at intervals of one day, from a simulation that
 336 used time steps of 300s . The computational domain was doubly periodic and f -plane, so we
 337 developed a spectral model for the adjoint equation in MATLAB. We adopted a comparable
 338 300s time step for the adjoint equation which, of course, required knowledge of the model
 339 state at comparable temporal resolution. This was obtained for any given one day interval
 340 by using the six days of MOM6 data centered on that day to interpolate via cubic splines the
 341 velocities and thickness to the required adjoint model times. The interpolated velocity and
 342 thickness data were used to compute kinetic energy and dissipation at the mass points of the
 343 model grid, and the pressure work at that point was estimated as the residual in the kinetic
 344 energy equation. Our estimates were checked against direct estimates of the pressure work
 345 which could be computed using the daily archived fields and the two were found to agree
 346 to a high degree of accuracy. In this way, we developed time series of the various inputs to
 347 the kinetic energy equation that balanced to machine precision, which in turn allowed us to
 348 balance our adjoint based kinetic energy budgets.

349 As is evident in (37), the evolving modified Green's functions are related to Lagrangian

measures of fluid displacement. This point is emphasized in Fig. 4 which compares the Green's functions corresponding to the beginning and the end of our experiment, i.e. to days 50 (left) and 220 (right). Comparatively speaking, the left hand side looks considerably more disorganized than the right hand side. This reflects the strongly interactive nature of the evolving fields, which moves particles considerable distances. The distribution on the left represents the density of the particles over the entire domain on day 50 that eventually, at day 220, end up in the square on the right. The multiple maxima appearing on the left are indicative of the primary merging vortices that between days 50 and 220 form the final vortex seen in Fig. 3.

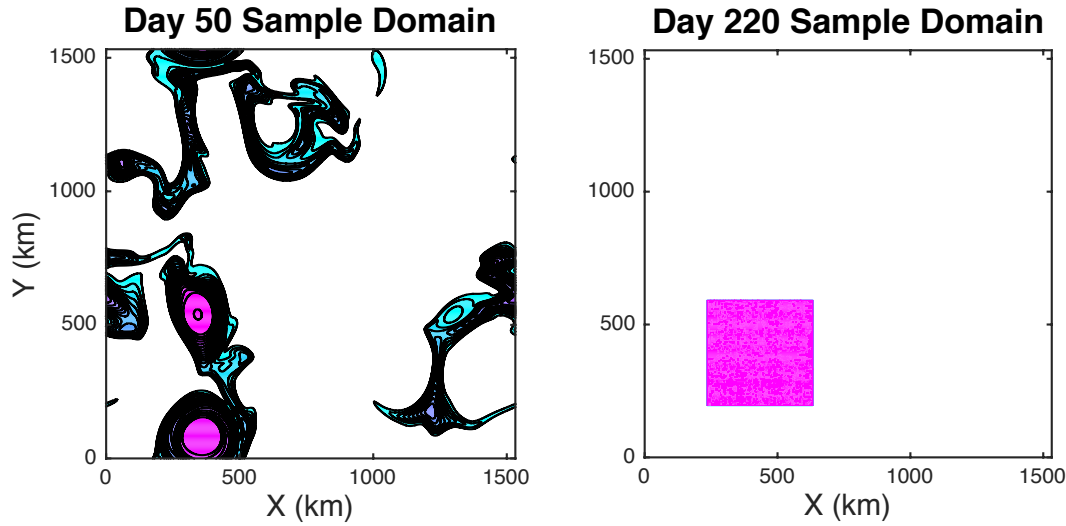


Figure 4: The modified Green's functions, defined by (37), from our numerical experiment at day 50 (left) and day 220 (right). The left panel essentially shows the distribution of the particles that end up in the square on the right. CI=.05e-4

Fourteen different sampling functions, $\pi_{Q,L_i}^{L_{i+1}}$ (see (38)), were developed, each designed to measure the average kinetic energy contained in the region indicated in Fig. 3 between two lengths, ranging from the full domain size (1536km) down to the grid scale. We used the first filter to remove the domain average, i.e.

$$\pi_{Q,L_j}^{L_k} = 1/A_o \quad (39)$$

where $L_j = 0\text{km}$, $L_k = 1536\text{km}$ and A_o is the domain area. Intermediate lengths were set to $(L_2 \rightarrow L_{13})=1200, 1000, 800, 700, 600, 500, 450, 400, 350, 300, 250$ and 150km . The adjoint problem appropriate to each of these sampling functions was solved to obtain fourteen different sets of $\Phi_{L_i}^{L_{i+1}}$ functions, and the kinetic energy, pressure work and dissipation fields were filtered using each of the associated filtering functions. This resulted in a 14×14 matrix for each of the kinetic energy and energy input fields, detailing how the various scale dependent quantities contributed to the final kinetic energy at a given time. We will refer to the results in terms of the bands associated with the initial $\Phi_{L_i}^{L_{i+1}}$ functions, as spelled out in Table 2.

Band No	Limits
1	Basin Average
2	1200-1536km
3	1000-1200km
4	800-1000km
5	700-800km
6	600-700km
7	500-600km
8	450-500km
9	400-450km
10	350-400km
11	300-350km
12	350-300km
13	300-350km
13	250-300km
14	150-250km
14	0-150km

Table 2: Band numbers and associated length scales.

372 For the purposes of this paper, we consider the transition from day 50 to day 220, i.e.
 373 over the entire interval of the vortex merger. We compare initial and final kinetic energy
 374 decompositions $\overline{\kappa_o^{L_i}}$, where

$$\overline{\kappa_o^{L_i}} = \sum_o^i \overline{\kappa_{L_o=0}^{L_i}} \quad (40)$$

375 as functions of length scale in Fig. 5. Note that some of the values are not positive. This is a
 376 consequence of (17), which insures that when summed all filtered contributions converge on
 377 the value of the energy in physical space. What is guaranteed to be positive is the final sum.
 378 Contributions from individual length scale bands can contribute negative values to achieve
 379 this goal.

380 The red line is $\overline{\kappa_o^{L_i}}$ of the initial kinetic energy within the square seen in Fig. 3(c).
 381 Although relatively flat, it does exhibit a peak in the range $L = (400 - 600)km$ which
 382 reflects the two vortices present at day 50. While indicative of the early energy distribution,
 383 a more telling decomposition comes from that found by subsampling the field according to
 384 the day 50 Green's function (see Fig. 4). This appears in the green line, which shows a
 385 weak dip in values at small length scales, followed by a steady growth. The final, blue, line
 386 is the decomposition associated with the day 220 state inside the square in Fig. 3(c). It is
 387 clear that, compared to both other curves, the kinetic energy has both grown considerably
 388 in amplitude, particularly at large L , which is consistent with an upscale cascade.

389 A more detailed view of the cross scale exchanges is shown in Fig. 6. Here we plot the
 390 decomposition of the large scale (band 2), intermediate scale (band 8) and small scale (band
 391 12) kinetic energy in the upper three panels. Each plot consists of 43 separate values. The
 392 first value is the band passed kinetic energy at day 220. This is followed in the next 14
 393 slots by the initial kinetic energy contributions from the various bands. Those values are

distinguished by a magenta axis. The next 14 slots are the various band passed contributions from the pressure work (cyan axis) and the final 14 slots (blue axis) are the contributions from dissipation. Each group of 14 contributions is also separated by a vertical black line. The solid black horizontal lines in each slot are the values of the contributions, and the red line starting from the second slot shows the cumulative sum of the values. As shown in (29), the sum of all the inputs should match the final band passed kinetic energy; equivalently, the final red value at slot 43 should match the black line in the first slot in amplitude. Note that this holds in all three plots. Finally, the three dashed green vertical lines mark the band corresponding to the band of the final kinetic energy for each of the initial kinetic energy, pressure work and dissipation. Bands left of the green line correspond to larger length scales and those to the right to shorter length scales.

The bottom panel connects the band number on the y-axis with the length scale range of that band on the x-axis.

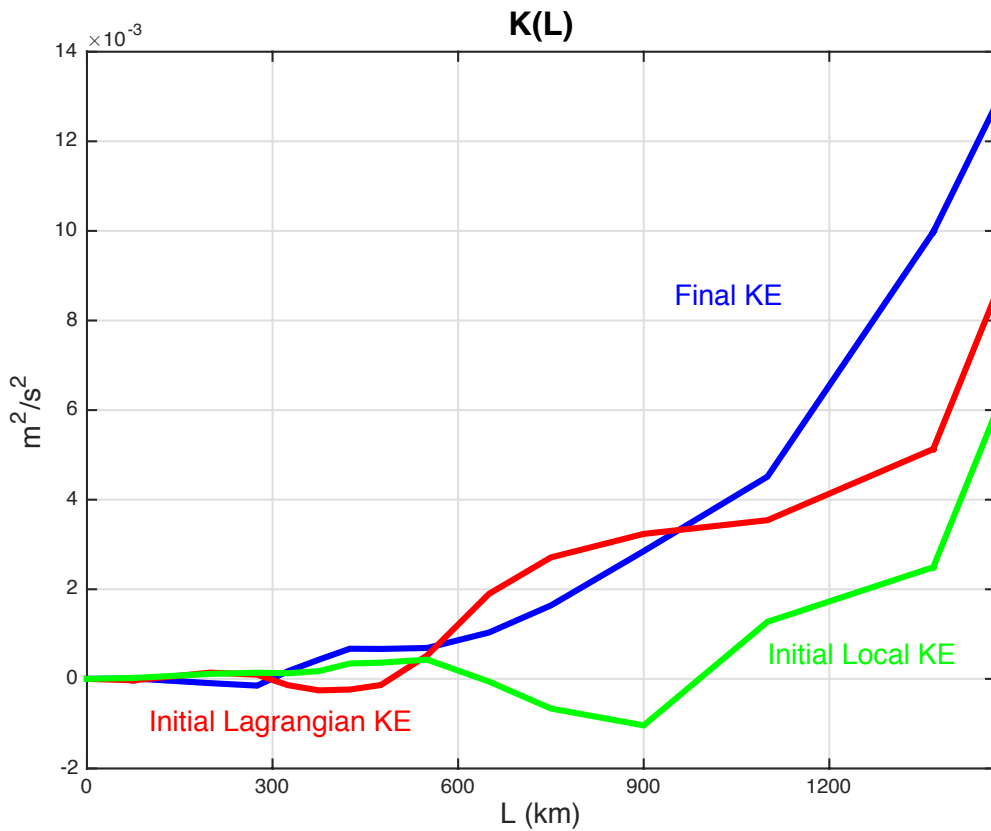


Figure 5: Initial length scale structure of the kinetic energy, $\overline{\kappa_o^{L_i}}$, compared to final length scale structure. The red line is based on the initial kinetic energy as sampled by the Lagrangian field in Fig. 4 (left), the green line is based on the initial kinetic energy inside the square in Fig 4 (right) and the blue line is based on the final kinetic energy inside the square in Fig. 4 (right). The final field (blue line) exhibits clear evidence of kinetic energy growth at longer scales.

407 3.1. Large Scales

408 For example, consider Fig. 6a. The first slot is occupied by

$$\overline{\kappa_{L_1}^{L_2}}(\mathbf{x}, t_o) = \int_{\mathbf{x}_o} K(\mathbf{x}_o, t_o) \pi_{Q, L_1}^{L_2}(\mathbf{x} - \mathbf{x}_o) d\mathbf{x}_o \quad (41)$$

409 which is the band 2 kinetic energy in the final state, with a value of roughly $5.5 \times 10^{-3} m^2/s^2$.
 410 A plot of the physical space structure of this quantity appears in Fig. 7d. The kinetic energy
 411 field at day 220 from which this filtered content is extracted appears above it in Fig. 7b.
 412 The next 14 slots, from slot 2 to 15, are occupied by

$$\int_{\mathbf{x}_o} \kappa(\mathbf{x}, 0)_{L_n}^{L_{n+1}} \Phi_{L_1}^{L_2}(\mathbf{x}, 0, \mathbf{x}_o; t_o) d\mathbf{x}_o \quad (42)$$

413 where

$$\kappa(\mathbf{x}, 0)_{L_n}^{L_{n+1}} = \int_{\mathbf{x}_1} K(\mathbf{x}_1, 0) \gamma_{L_n}^{L_{n+1}}(\mathbf{x} - \mathbf{x}_1) d\mathbf{x}_1 \quad (43)$$

414 is the initial kinetic energy content contained in band n (see Table 2). The dashed green
 415 line marks the third slot, which is the second band of the initial kinetic energy. This is
 416 the same band appearing in the first slot, and a physical space picture of this transfer term
 417 appears in Fig. 7c. The day 50 kinetic energy field from which this term is extracted by (42)
 418 appears above it in Fig. 7a. It is clear from comparing the black line in the green dashed
 419 slot to the black line in the first slot from fig. 6a that this band has grown in kinetic energy
 420 over the experiment, from an initial value of $1.3 \times 10^{-3} m^2/s^2$ to roughly $5.5 \times 10^{-3} m^2/s^2$.
 421 The values in the remaining slots in the kinetic energy zone represent the contributions from
 422 shorter length scales in the initial kinetic energy to the band 2 final kinetic energy structure.
 423 The next four values in the initial kinetic energy zone are positive, indicating a transfer of
 424 smaller scales upward. The remaining slots are filled with very small values. The cumulative
 425 red line indicates the total transfer to band 2 final kinetic energy from initial kinetic energy
 426 is roughly $3.3 \times 10^{-3} m^2/s^2$, with the biggest single contributor being the local band 2. In
 427 summary, this plot suggests an upscale kinetic energy to kinetic energy cascade.

428 The slots from 16 to 29 are occupied by

$$\int_o^{t_o} \int_{\mathbf{x}} (-pw(\mathbf{x}, t)_{L_n}^{L_{n+1}}) \Phi_{L_1}^{L_2}(\mathbf{x}, t, \mathbf{x}_o; t_o) d\mathbf{x}_o dt \quad (44)$$

429 where

$$pw(\mathbf{x}, t)_{L_n}^{L_{n+1}} = \int_{\mathbf{x}_1} (up_x + vp_y)(\mathbf{x}_1, t) \gamma_{L_n}^{L_{n+1}}(\mathbf{x} - \mathbf{x}_1) d\mathbf{x}_1 \quad (45)$$

430 is the pressure work performed in band n at time t of the calculation. The green dashed
 431 line falls in slot 17 because that band corresponds to the band appearing in the first slot.
 432 The values in the remaining slots represent contributions to band 2 final kinetic energy from
 433 other bands in the pressure work occurring along the fluid trajectory. As can be seen from
 434 the red lines, pressure work is considerably more active across the bands than kinetic energy.
 435 The green dashed slot contains a negative value, indicating a net loss of kinetic energy
 436 by the pressure work in this band. However the next several slots are positive, indicative

437 of an upscale cascade of energy due to pressure work, and in total, these transfers are
438 considerably stronger than the in-band loss. In total, pressure work elevates kinetic energy
439 by $3.8 \times 10^{-3} m^2/s^2$, and is roughly 3 – 4 times larger than the kinetic to kinetic transfer,
440 with most of the transfers coming from smaller scales. This result is somewhat surprising,
441 as most previous studies have focussed on kinetic to kinetic transfers. Contributions from
442 other sources, such as pressure work, have not received as much attention. Here they are
443 dominant.

444 Last, we come to the dissipative contributions, appearing in slots 30 to 43. Here, the
445 surprise is that the net dissipative effects acting on band 2 are relatively large. Over all
446 scales, the net effect is slightly less than $-1.3 \times 10^{-3} m^2/s^2$, although the total is dominated
447 by the in-band, band 2, dissipative impact of slightly more than $-1.3 \times 10^{-3} m^2/s^2$. The
448 reason this is unexpected is that band 2, from $1536 - 1200 km$, is a large scale band, and
449 dissipation is dominantly a small scale process. This is certainly true as well in the present
450 simulation, as is seen in Fig. 8a of the modeled dissipation field at day 135. However,
451 dissipation is broadly distributed and occurs at locations governed by the large scale, so that
452 when filtered, dissipation imprints importantly on the evolution. This appears in Fig. 8b
453 which is the dissipation field at day 135 filtered through band 2.

454 3.2. Intermediate and Small Scales

455 Band 8, in Fig. 6b, loses kinetic energy over the simulation, as can be seen by comparing
456 the black line in the first slot with that in the first green dashed slot. However, the scale of this
457 loss is close to two orders of magnitude smaller than those described for band 2. Essentially,
458 this is an inert band in regards to kinetic to kinetic exchanges. Across the bands, initial
459 kinetic inputs to final kinetic energy are quite small, at a net value of $3 \times 10^{-6} m^2/s^2$. Note
460 however that pressure work is quite active across all bands. Larger scale bands, to the left
461 of the green dashed line in the pressure work zone, tend to be positive. This is indicative
462 of a down-scale transfer of energy from larger scales to band 8. However, smaller scales
463 tend to be negative in amplitude, and overall comparable in size to the contributions from
464 the larger scales. The net effect of pressure work across all bands, is negative, at a value
465 of $-1.7 \times 10^{-5} m^2/s^2$, indicative of a net transfer to small scales. Band 8, with respect to
466 pressure work, acts like a pass-through, allowing energy from larger scales to move through
467 to smaller scales, while adding a small amount to the net. In this intermediate scale band,
468 the principal signal is a down-scale contribution to kinetic energy.

469 Finally, band 12, in Fig. 6c, is also a band of relatively weak energy transfers, if still
470 stronger than band 8. Overall, there is a stronger kinetic energy loss at these small scales,
471 roughly $-5.5 \times 10^{-5} m^2/s^2$, most of which, $-4.0 \times 10^{-5} m^2/s^2$ is accounted for by losses to
472 larger length scales. This is indicative of a kinetic to kinetic upscale transfer. Once again, it
473 is seen the pressure work to kinetic energy transfers are far more active. While the net effect
474 is relatively small, $-1 \times 10^{-5} m^2/s^2$, it is the result of large transfers of both signs across the
475 length scale spectrum. A clear pattern does not emerge. Losses and gains to other length
476 scale bands of both larger and small character occur. Perhaps the safest interpretation is
477 that the weak values involved in this band indicate it responds erratically to the conditions
478 imposed on it by the energetically dominant larger length scales.

479 Time histories of two of the pressure work energy transfers is shown in Fig. 9, i.e. those
480 for band 2 to band 2 and for band 3 to band 2. These are amongst the most active pressure

481 work bands seen in Fig. 6 and, despite their similarity in length scales, show opposite trends.
482 The band 2 to band 2 transfer appears on the left. Early in the experiment, pressure work
483 adds to kinetic energy, but the trends reverses around day 120, and pressure work depletes
484 kinetic energy strongly to day 220. The last 100 days are thus associated with a large scale
485 tendency for flow to be directed towards high pressures and away from low pressures. Fig.
486 9b, the pressure work contribution of band 3 to band 2, shows the opposite trend. Pressure
487 work persistently builds kinetic energy through most of the experiment, except for the period
488 from day 100 to day 120. Towards the end, the net levels to a constant value, equivalent to
489 the cessation of pressure work contributions between bands.

490 These tendencies are explained in part by examining the anatomy of the pressure work
491 contributions. For this we show in Fig. 10 the pressure work field as it appears to band 2
492 at day 200, for the two bands 2 and 3. On the left is the pressure work as seen by band
493 2, having been filtered through band 2. Note that the structure is dominated by relatively
494 large scale negative values. These are zones dominated by cyclones, and hence low pressures.
495 The negative pressure work values indicate flows away from the low pressure centers, which
496 is a flow field designed to bring the lows together. As a result, the negative pressure work
497 at largest scales is a signal of vortex merger. In contrast, the pressure work filtered through
498 band 3, as it appears to band 2 appears on the right. Here, the distribution consists much
499 more evenly of both highs and lows of comparable magnitude. Day 200 is relatively late in
500 the merger event, and is a point where on these scales of band 3, the fields are becoming
501 relatively symmetrized. As a result, the net pressure work from this band is quite small,
502 consistent with the late parts of the time series in Fig. 9 (right), where the time history of
503 integrated pressure work has leveled off.

504 4. Summary

505 A new method for computing cross-scale energy transfers in fluid flows has been described
506 and applied to a well-known example. The technique has both Lagrangian and Eulerian
507 forms. In this paper, we mostly examine the former method, which exploits the Lagrangian
508 nature of kinetic energy evolution to relate kinetic energy at any one location and time
509 to its flow history. The Lagrangian history is computed by solving an adjoint equation
510 obtained by a classical Green's function approach. The scale content of the final kinetic
511 energy structure can be obtained by solving a filtered version of the adjoint equation, and
512 projecting the kinetic energy field onto the result. In addition the same filter used on the
513 Green's function equation can be used to diagnose the scale dependent inputs to the kinetic
514 energy evolution, such as pressure work and dissipation, in a relatively straightforward way.
515 This leads rather naturally to a quantification of how energy from one band of length scales
516 transfers to another during the nonlinear evolution of the flow. The procedure also allows for
517 a diagnosis of the nature of the energy transfers, eg kinetic to kinetic or kinetic to pressure
518 work, as well as examination of how the transfers are structured in time and space. While we
519 have here focussed on kinetic energy, the same approach can be applied to potential energy
520 evolution.

521 We have applied the procedure to the classic problem of vortex merger in a stratified fluid.
522 The well known MOM6 model was deployed in a four layer isopycnal configuration and with
523 an initial condition consisting of a sequence of undulations in second layer thickness. The

524 system evolution proceeds with like signed vortices merging and opposite signed vortices
525 pairing up and propagating. We analyzed a particular merger event in detail.

526 The subsequent analysis showed the expected result that kinetic energy exhibits an up-
527 scale cascade; however, the procedure also illustrates several somewhat novel aspects about
528 merger. Perhaps most significantly, the primary energy transfers involve pressure work to
529 kinetic energy exchanges, rather than kinetic to kinetic energy exchanges. This result com-
530plements several published studies of upscale energy transfers which have focussed on Fourier
531 transforms of the nonlinear advection terms in the momentum equations by emphasizing the
532 role played by pressure work. Dissipation also emerged as a surprisingly large effect on larger
533 scale energy exchanges. This was due in part to the tendency for the larger scale flow to or-
534 ganize regions of small scale dissipation, so that the large-scale projection of dissipation was
535 substantial. Also, several of the intermediate ranges in an integral sense were relatively inert,
536 in that initial and final kinetic energies were often quite similar; however those same ranges
537 were found to be very dynamically active, and acted as pass-throughs, receiving potential
538 energy from smaller scales and passing them along to larger scales. Finally, the diagnoses
539 identify the critical points in time when exchanges are at their peak, and allows for an exam-
540 ination of the events associated with the exchanges. Spatial information about the nature
541 of the exchanges is also provided and allows for a diagnosis of the involved mechanisms.

542 The example problem considered here is highly idealized, with an isotropic setting, doubly
543 periodic boundaries and an unobstructed geometry. The promise of the technique, however, is
544 that it potentially generalizes in a straightforward way to realistic ocean simulations, in which
545 the flows are highly anisotropic and inhomogeneous, and the domains are often geometrically
546 complex. The examination of such regions, such as the Gulf Stream, the Kuroshio and other
547 major ocean currents is of importance to the understanding of the global ocean energy cycle.
548 It will be of great interest to see what new light this method might cast on such regions.

549 Acknowledgments

550 This work was supported through NSF grants OCE-1537304, OCE-1829856, OCE-1941963
551 and the French ‘Make Our Planet Great Again’ program managed by the Agence Nationale
552 de la Recherche under the Programme d’Investissement d’Avenir, with the reference ANR-18-
553 MPGA-002. Computations were performed on the National Computational Infrastructure,
554 Canberra, AU, which is funded by the Australian Government. The authors in particular
555 would like to recognize many interesting and relevant conversations with L. Zanna, B. Ar-
556 bic and B. Fox-Kemper. We have also benefitted greatly from very thorough and careful
557 reviews of our manuscript by three anonymous referees and K. Srinivasan. The positive im-
558 pact these reviews have had on our paper can not be overstated. We are grateful to JAMES
559 editor Stephen Griffies for his usual careful and professional handling of our manuscript and
560 his insightful observations.

561 The simulation data for the vortex merger experiment is available at doi 10.6084/m9.figshare.12485426.

562 Appendix A. Basis Functions for Arbitrary Domains

563 Trigonometric functions form the obvious filtering basis set for unbounded and simple
564 domains. Unfortunately, such domains are rarely associated with realistic problems, so it

565 is necessary to consider a generalization when filtering a variable in a realistic setting. The
 566 purpose of this appendix is to suggest one method to develop an appropriate basis set. We
 567 stress that the example in the main part of the paper uses classical trigonometric functions
 568 and doesn't involve any of the more elaborate filters computed here.

569 The key property of trigonometric functions that leads to their utility is (18). In turn, the
 570 demonstration of this property for trigonometric functions depends on their orthonormality,
 571 i.e. that

$$\int_{-\infty}^{\infty} f_n(\mathbf{x}) f_m(\mathbf{x}) d\mathbf{x} = \delta_{n,m} \quad (\text{A.1})$$

572 where $f_n(\mathbf{x})$, $f_m(\mathbf{x})$ are two trigonometric functions characterized by eigenvalues n , m and
 573 $\delta_{n,m}$ is the Kronecker delta function. We wish to retain these properties while developing
 574 basis functions appropriate to more general settings.

575 It is widely recognized that orthonormal functions are often developed from dynamical
 576 equations. Here we make the conscious decision to avoid any basis set developed from dy-
 577 namical considerations. The reason for this is we want to make a scale dependent statement
 578 only, and not a statement about any preconceived dynamical content. To this end, consider
 579 the classical Helmholtz equation

$$\nabla^2 \psi + k^2 \psi = 0 \quad (\text{A.2})$$

580 In the presence of homogeneous boundary conditions, the solution of this equation is $\psi = 0$,
 581 except possibly for special values of the constant k , making it an eigenvalue problem. By
 582 construction, the eigenvectors of (A.2) are the eigenvectors of the Laplacian operator. If one
 583 is in possession of two separate eigenvectors of (A.2), say ψ_m and ψ_n , they are automatically
 584 orthogonal, as we now demonstrate. First, insert one of these eigenvectors into (A.2) and
 585 multiply by the other

$$\psi_n \nabla^2 \psi_m + \psi_n k_m^2 \psi_m = 0 \quad (\text{A.3})$$

586 where k_m is the eigenvalue associated with ψ_m . Integrating over the domain in question

$$\int_S (\psi_n \nabla \psi_m - \psi_m \nabla \psi_n) + \int_V (\psi_m \nabla^2 \psi_n + \psi_m k_m^2 \psi_n) dV = 0 \quad (\text{A.4})$$

587 where S is the domain boundary enclosing the integration volume V . In the presence of
 588 homogeneous boundary conditions and introducing the remaining eigenvalue k_n

$$(k_m^2 - k_n^2) \int_V \psi_m \psi_n dV = 0 \quad (\text{A.5})$$

589 Eq. (A.2) being a Sturm-Liouville equation possesses an infinity of eigenvector/eigenvalue
 590 pairs that can be ordered from smallest to largest so, in general, the factor multiplying the
 591 integral on the left hand side of (A.5) does not vanish. Thus, by construction, the eigenvalues
 592 are orthogonal. Enforcing

$$\int_V \psi_m^2 dV = 1 \quad (\text{A.6})$$

593 insures they are also suitably normalized. Further classical analysis shows arbitrary func-
 594 tions in V can be represented by an appropriate superposition of the eigenfunctions (in a

595 least squares sense) where the coefficients of the representation are computed by exploiting
596 orthonormality.

597 In regards to the length scale, L , we would associate with any particular eigenfunction,
598 the form of the Helmholtz equation suggests

$$L \approx k^{-1} \quad (\text{A.7})$$

599 We will see in multiple dimensions that this simple relationship is problematic.

600 While for irregular domains with islands and topography, the solutions cannot generally
601 be written down, they can be developed in relatively straightforward numerical ways. As
602 an example, consider the domain shown in Fig. A.11, consisting of a single circular island
603 inside of an otherwise square domain. The Laplacian operator is discretized using a five point
604 stencil. Periodic boundary conditions are placed on the outer edge of the domain and the
605 eigenfunctions are required to vanish on the island boundary. These are conditions consistent
606 with the orthogonality of the resulting Helmholtz solutions and are entirely reflected in the
607 details of the stencil coefficients. In principle, the coefficients can be formed into a $nx \times ny$ by
608 $nx \times ny$ square matrix, where nx , ny are the lengths of the domain in the east-west, north-
609 south directions, respectively. For the present calculation, $nx = ny = 70$ and grid spacing
610 dx , $dy = 5m$ is isotropic. In fact, this does not account for the island, inside of which are
611 several of the regularly spaced grid points, but which represent locations inaccessible to the
612 fluid. It is necessary to remove those points, resulting in slightly smaller matrix, the regular,
613 pentadiagonal structure of which is then interrupted.

614 This matrix can be fed into a standard eigenvalue extraction routine; we used the function
615 ‘eig’ in MATLAB. The gravest and tenth-most gravest eigenmodes appear in Fig. A.12;
616 these are associated with eigenvalues $k_1^2 \approx 10^{-4} m^{-2}$ on the left and $k_{10}^2 \approx 1.4 \times 10^{-3} m^{-2}$, or
617 equivalently $L_k \approx 200m$ (left) and $L_{10} \approx 52m$ (right). It is easy to associate a length scale
618 of 200m with the former, but the latter also measures comparable length scales while being
619 spatially considerably more complex. It is thus not straightforward to simply connect the
620 eigenvalue size and the associated length scale. This is due to the multiple spatial dimensions
621 involved in the analysis, and arises in the unbounded domain using simple trigonometric
622 functions as well. For example, high wavenumbers in the meridional direction coupled to
623 low wavenumbers in the zonal direction can be associated with eigenvalues very similar
624 to comparable wavenumbers of intermediate values distributed symmetrically in the two
625 directions. We recommend a different way to associate length scales to the analysis below.

626 We now demonstrate these functions satisfy constraint (18). Exploiting orthonormality,
627 we anticipate

$$\sum_n a_n \psi_n(\mathbf{x}) = \delta(\mathbf{x} - \mathbf{x}_o) \quad (\text{A.8})$$

628 where

$$a_n = \psi_n(\mathbf{x}_o) \quad (\text{A.9})$$

629 The result of evaluating this formula using the present eigenfunctions appears in Fig. A.13(top
630 left), where the source point $\mathbf{x}_o = (50m, 150m)$, i.e. just south of the island. Clearly, we
631 have reproduced to within domain discretization a Dirac delta function. The analysis in the
632 main part of the paper, however, emphasized the use of integrals of filters between two length
633 scales. We present in Fig. A.13(top right) the result of summing all the eigenfunctions below

634 a given eigenvalue. This corresponds to (28), in particular to $\gamma_o^{L_j}$ for the 100th eigenvalue
 635 ($k_{100}^2 \approx .012$). Cross sections of the sampling function on the dashed lines in Fig. A.13b
 636 appear in the two lower panels. Note that the sampling function γ_{100} avoids the island,
 637 as seen in Fig. A.13(bottom left), while maintaining a qualitative resemblance to the *sinc*
 638 function (Fig. A.13(bottom right)). The length scale L associated with the eigenvalue is
 639 roughly 90m, which corresponds well to the length scale of the sampling function, particu-
 640 larly as suggested by the distance separating the neighboring highest positive lobes seen in
 641 Fig. A.13. As suggested by this example, we recommend associating length scales L with
 642 sums of eigenfunctions corresponding to ranges of the eigenvalues.

643 Clearly this technique, while promising, is in need of considerable study.

644 Appendix B. Eulerian Kinetic Energy Exchanges

645 This paper deals primarily with the Lagrangian version of the kinetic energy equation,
 646 somewhat in a manner reminiscent of Nagai et al. (2015) and Shakespeare and Hogg (2017).
 647 However, an Eulerian statement can be made as well and the formulation is outlined here.
 648 Starting with (29), the final time t_o is chosen to be very small, such that

$$\kappa_{L_j}^{L_k}(\mathbf{x}_1, t_o) = \int_{\mathbf{x}} \Gamma_{L_j}^{L_k} K(\mathbf{x}, 0) d\mathbf{x} + \left(\int_{\mathbf{x}} R(\mathbf{x}, t) \Gamma_{L_j}^{L_k} d\mathbf{x} \right) t_o \quad (\text{B.1})$$

649 where we have neglected boundary contributions. Integrating (27) over a small time interval
 650 centered on t_o results in

$$\Gamma_{L_j}^{L_k}(\mathbf{x}, t_o; \mathbf{x}_1, t_o) = \gamma_{L_j}^{L_k}(\mathbf{x} - \mathbf{x}_1) \quad (\text{B.2})$$

651 so (B.1) can be rewritten

$$\int_{\mathbf{x}} \frac{\partial}{\partial t} (\Gamma_{L_j}^{L_k} K(\mathbf{x}, t)) d\mathbf{x} = \int_{\mathbf{x}} R(\mathbf{x}, t) \Gamma_{L_j}^{L_k} d\mathbf{x} \quad (\text{B.3})$$

652 Using the chain rule converts (B.3) to

$$\int_{\mathbf{x}} \left(K \frac{\partial}{\partial t} \Gamma_{L_j}^{L_k} + \gamma_{L_j}^{L_k} \frac{\partial}{\partial t} K \right) d\mathbf{x} = \int_{\mathbf{x}} R(\mathbf{x}, t) \Gamma_{L_j}^{L_k} d\mathbf{x} \quad (\text{B.4})$$

653 Finally, substituting with (26) and integrating by parts leads to

$$\int_{\mathbf{x}} \gamma_{L_j}^{L_k} \frac{\partial}{\partial t} K d\mathbf{x} = \int_{\mathbf{x}} \gamma_{L_j}^{L_k} (-\nabla \cdot \mathbf{u} K + \nabla \cdot (\nu \nabla K) + R) d\mathbf{x} \quad (\text{B.5})$$

654 The left hand side is recognized as the filtered version of the time rate kinetic energy change,
 655 and the right hand side breaks it up into advective, diffusive, pressure work and dissipative
 656 contributions. The filter $\gamma_{L_n}^{L_{n+1}}$ is independent of time, so the left hand side of (B.5) can be
 657 rewritten

$$\int_{\mathbf{x}} \gamma_{L_j}^{L_k} \frac{\partial}{\partial t} K d\mathbf{x} = \frac{\partial}{\partial t} \int_{\mathbf{x}} \gamma_{L_j}^{L_k} K d\mathbf{x} = \frac{\partial}{\partial t} \kappa_{L_j}^{L_k} \quad (\text{B.6})$$

658 Thus the Eulerian version of the present analysis concerns the time rate of change of the
 659 band passed kinetic energy. The kinetic energy appearing in the advective and diffusive

660 terms can be similarly decomposed, which in turn yield formulae expressing the exchange
 661 of kinetic energy between bands involving spatial operations on the filter. For example, the
 662 advective contribution becomes

$$\int_{\mathbf{x}} \gamma_{L_j}^{L_k} (-\nabla \cdot \mathbf{u} K) d\mathbf{x} = \int_{\mathbf{x}} \gamma_{L_j}^{L_k} (-\nabla \cdot \mathbf{u} \int_{\lambda} K_{\lambda} d\lambda) d\mathbf{x} \quad (\text{B.7})$$

663 After some algebra and modifying the order of integration

$$\int_{\mathbf{x}} \gamma_{L_j}^{L_k} (-\nabla \cdot \mathbf{u} K) d\mathbf{x} = \int_{\lambda} \int_{\mathbf{x}} \gamma_{L_j}^{L_k} \mathbf{u}(\mathbf{x}) \int_{\mathbf{x}_{\alpha}} K(\mathbf{x}_{\alpha}) \nabla f_{\lambda}(\mathbf{x}_{\alpha} - \mathbf{x}) d\mathbf{x}_{\alpha} d\mathbf{x} d\lambda \quad (\text{B.8})$$

664 In this Eulerian view, advective contributions appear explicitly. This procedure is somewhat
 665 like that described in Aluie et al. (2018), although we work directly in kinetic energy rather
 666 than the momentum equations. Last, this result can also be obtained by filtering the Eulerian
 667 kinetic energy equation directly.

668 Appendix C. Potential Energy

669 Vertical buoyancy transport connects potential and kinetic energies, and this is intro-
 670 duced into (3) by adding and subtracting $w p_z$, which yields

$$K_t + \nabla \cdot \mathbf{u} K = -\nabla \cdot \mathbf{u} p + w b - \epsilon + \nabla \cdot (\nu \nabla K) \quad (\text{C.1})$$

671 where b is buoyancy and the velocity is fully three dimensional. For a linear equation of
 672 state, the quantity $w b$ can be related to $h = -b z$ via

$$h_t + \nabla \cdot \mathbf{u} h = -w b + \nabla \cdot \kappa \nabla h + 2\kappa b_z \quad (\text{C.2})$$

673 where κ is diffusivity.

674 For a nonlinear equation of state, the choice for h of ‘dynamic enthalpy’ (Young (2010))

$$h = \int_{P_o}^P \frac{b}{g \rho_o} dP \quad (\text{C.3})$$

675 where ρ_o is a reference density, g gravity, $P = -\rho_o g z$ is static pressure and P_o is a reference
 676 surface pressure, leads to a generalized form of (C.2). This equation involves a lot of terms
 677 and is not written down here.

678 Note that (C.2) can be rewritten as

$$h_t + \nabla \cdot \mathbf{u} h - \nabla \cdot \kappa \nabla h = \chi \quad (\text{C.4})$$

679 where $\chi = -w b + 2\kappa b_z$ represents the ‘sources’ of potential energy. The form of (C.4) is
 680 identical to that of (4), so the previous analysis and results all apply to potential energy. If
 681 the fluid is modeled assuming identical diffusivity and viscosity (i.e. a Prandtl number of 1),
 682 the analysis in this paper can be applied to the sum of kinetic and potential energy. In any
 683 case, potential energy can always be analyzed separately from kinetic and the two connected
 684 through their common quantity, $w b$.

685 **Appendix D. Isopycnal fluids**

686 If one works in a layered model, as the example in the main part of the paper, the
687 momentum equations change slightly so, for example, the zonal momentum equation becomes

$$u_t + uu_x + vu_y - fv = -M_x - \frac{\nabla \cdot F^x}{h} \quad (\text{D.1})$$

688 where M is the Montgomery potential

$$M = p - bz \quad (\text{D.2})$$

689 and F^x represents the viscous fluxes of zonal momentum. Notation is otherwise the same
690 as in (1). The kinetic energy equations formed from these momentum equations, employing
691 the usual statements for viscous fluxes, is

$$K_t + uK_x + vK_y = -uM_x - vM_y - \epsilon + \frac{1}{h} \nabla_h \cdot (h\nu \nabla_h K) \quad (\text{D.3})$$

692 where h is layer thickness and the subscript ‘h’ denotes ‘horizontal’. Following the Green’s
693 function formalism eventually leads to

$$K(\mathbf{x}_o, t_o) = \int_{\mathbf{x}} G(\mathbf{x}, 0; \mathbf{x}_o, t_o) K(\mathbf{x}, 0) d\mathbf{x} + \int_t \int_{\mathbf{x}} G(\mathbf{x}, 0; \mathbf{x}_o, t_o) R(\mathbf{x}, 0) d\mathbf{x} dt \quad (\text{D.4})$$

694 where

$$R = -uM_x - vM_y - \epsilon \quad (\text{D.5})$$

695 and

$$G_t + \nabla \cdot \mathbf{u}_h G = \nabla_h \cdot (\nu h \nabla_h \frac{G}{h}) - \delta(\mathbf{x} - \mathbf{x}_o, t - t_o) \quad (\text{D.6})$$

696 These are the equations used in the analysis of the MOM6 results.

697 **References**

698 **References**

- 699 Aluie, H., Hecht, M., Vallis, G., 2018. Mapping the energy cascade in the North Atlantic
700 Ocean: The coarse-graining approach. *Journal of Physical Oceanography* 48, 225–244.
- 701 Arbic, B., Muller, M., Richman, J., Shriver, J., Morten, A., Scott, R., Serazin, G., Penduff,
702 T., 2014. Geostrophic turbulence in the frequency-wavenumber domain: Eddy-driven low-
703 frequency variability. *Journal of Physical Oceanography* 44, doi:10.1175/JPO-D-13-054.1.
- 704 Arbic, B., Scott, R., Flierl, G., Morten, A., Richman, J., Shriver, J., 2012. Nonlinear cascades
705 of surface oceanic geostrophic kinetic energy in the frequency domain. *Journal of Physical
706 Oceanography* 42, 1577–1600.
- 707 Berloff, P., McWilliams, J., 1999. Large-scale, low-frequency variability in wind-driven ocean
708 gyres. *Journal of Physical Oceanography* 29, 1925–1949.

- 709 Charney, J., 1971. Geostrophic turbulence. *Journal of Atmospheric Science* 28, 1087–1095.
- 710 Dijkstra, H., Molemaker, M., 1999. Imperfections of the North Atlantic wind-driven ocean
711 circulation: Continental geometry and windstress shape. *Journal of Marine Research* 57,
712 1–28.
- 713 Ferrari, R., Wunsch, C., 2009. Ocean circulation kinetic energy - reservoirs, sources and
714 sinks. *Ann. Rev. Fluid Mech.* 41, 253–282.
- 715 Fjortoft, R., 1953. On the changes in the spectral distribution of kinetic energy for two-di-
716 mension, nondivergent flow. *Tellus* 5, 225–230.
- 717 Holland, W., 1978. The role of mesoscale eddies in the general circulation of the ocean -
718 numerical experiments using a wind-driven quasi-geostrophic model. *Journal of Physical
719 Oceanography* 8, 363–392.
- 720 Kelley, D., Allshouse, M., Ouellette, N., 2013. Lagrangian coherent structures
721 separate dynamically distinct regions in fluid flows. *Physical Review E* 88,
722 doi:10.1103/PhysRevE.88.013017.
- 723 Kraichnan, R., 1964. Decay of isotropic turbulence in the direct-interaction approximation.
724 *Physics of Fluids* 7, doi:10.1063/1.1711319.
- 725 Kraichnan, R., 1967. Intertial ranges in two-dimensional turbulence. *The Physics of Fluids*
726 10, doi:10.1063/1.1762301.
- 727 Nagai, T., Tandon, A., Kunze, E., Mahadevan, A., 2015. Spontaneous generation of near-
728 inertial waves by the Kuroshio Front. *Journal of Physical Oceanography* 45, 2381–2406.
- 729 Scott, R., Arbic, B., 2007. Spectral energy fluxes in geostrophic turbulence: Implications for
730 ocean energetics. *Journal of Physical Oceanography* 37, 673–688.
- 731 Scott, R., Wang, F., 2005. Direct evidence of an oceanic inverse kinetic energy cascade from
732 satellite altimetry. *Journal of Physical Oceanography* 35, 1650–1666.
- 733 Shakespeare, C., Hogg, A., 2017. Spontaneous surface generation and interior amplification
734 of internal waves in a regional-scale ocean model. *Journal of Physical Oceanography* ,
735 doi:10.1175/JPO-D-16-0188.1.
- 736 Wunsch, C., Ferrari, R., 2004. Vertical mixing, energy, and the general circulation of the
737 oceans. *Ann. Rev. Fluid Mech.* 36, doi:10.1146/annurev.fluid.36.050802.122121.
- 738 Young, W., 2010. Dynamic enthalpy, conservative temperature, and the seawater boussinesq
739 approximation. *Journal of Physical Oceanography* 40, 394–400.

740 **References**

741

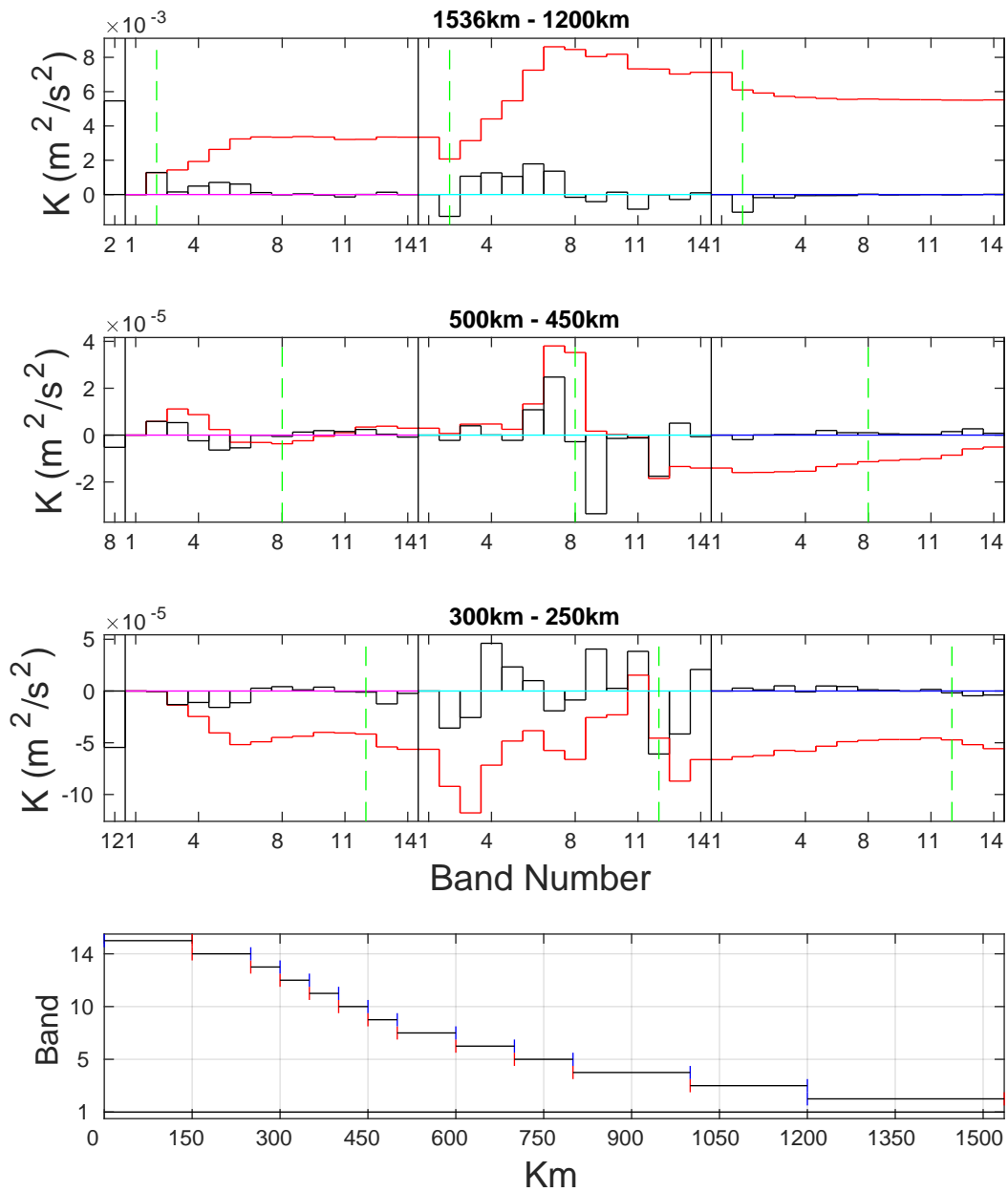


Figure 6: Three kinetic energy decompositions corresponding to bands 2 (upper), 8 (next upper) and 12 (next lower). Vertical black lines limit the final kinetic energy in the band, the contributions to that band from the 14 bands of the initial kinetic energy, pressure work and dissipation, respectively. Horizontal black lines denote values of the quantity and the red line is the cumulative sum, moving to the right, of the various contributions. The abscissa denotes band number and the ordinate is energy in m^2/s^2 . The bottom plot connects the band number on the y-axis to the length scales within that band, appearing on the x-axis in km.

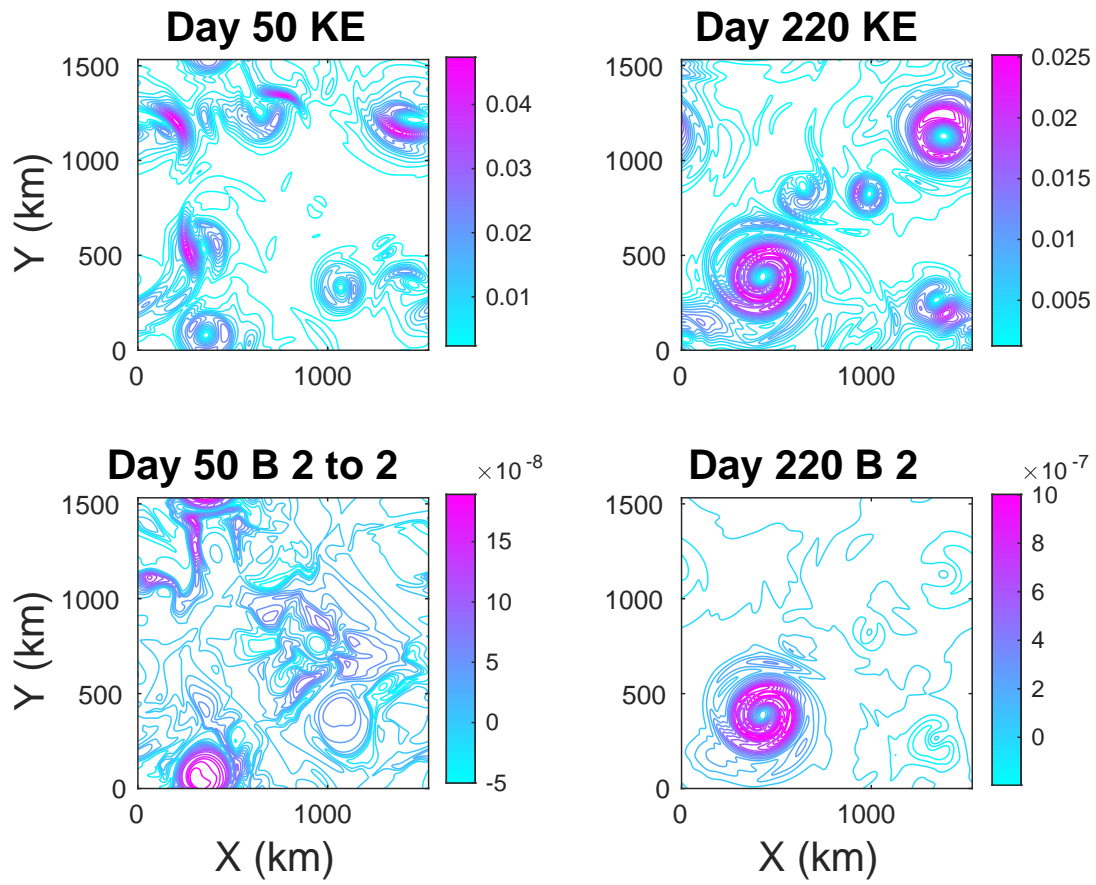


Figure 7: The kinetic energy distributions in layer 2 from our model run appear in the upper row (day 50 (left) and day 220 (right)). The kinetic energy transfer in band 2 from day 50 to day 220 appears in the lower left, and the day 220 kinetic energy content in band 2 appears in the lower right.

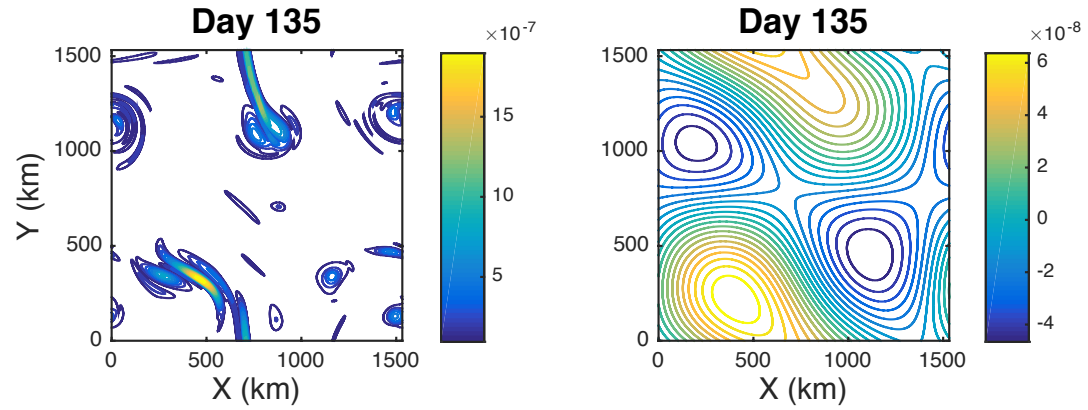


Figure 8: The distribution of dissipation at day 135 appears on the left. Note that it is concentrated into small areas. Dissipation as it affects band 2 appears on the right. Although this is a large scale mode, dissipation is still a major input to the kinetic energy development, as is seen in Fig. 6.

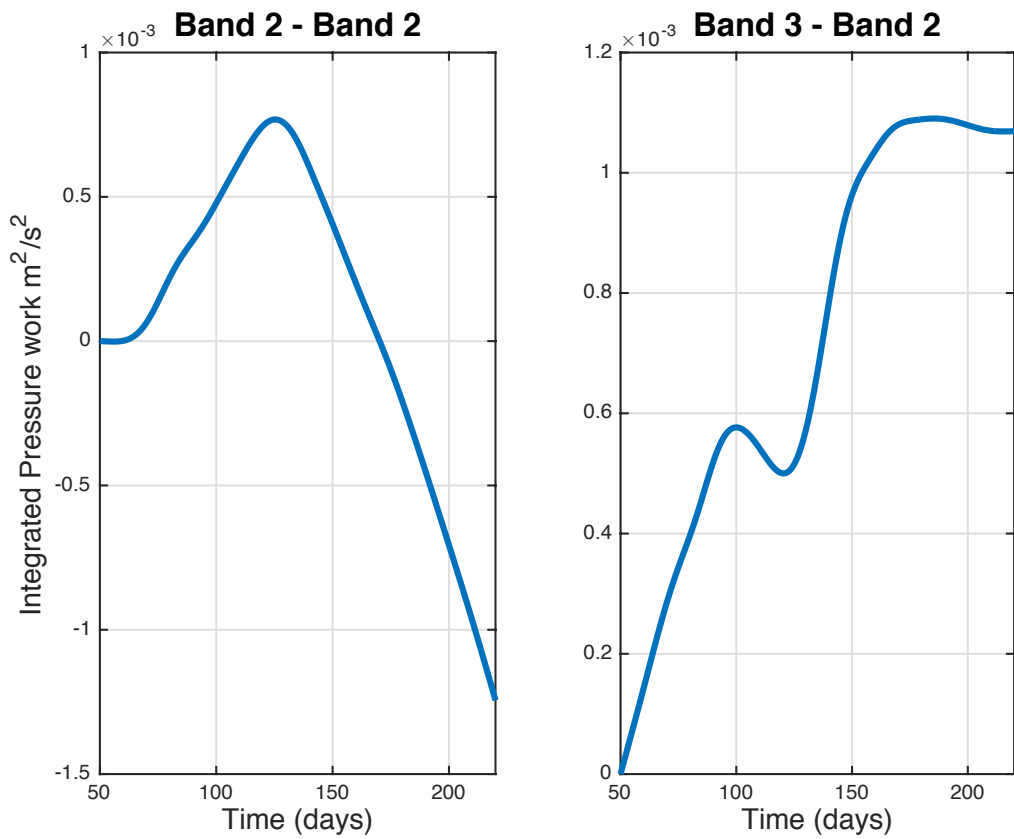


Figure 9: Timeseries of the pressure work input to kinetic energy. The pressure effect on band 2 of band 2 appears on the left and on band 2 due to band 3 on the right. Note the difference in scale on the y-axis. The net pressure work between these two cases are opposites, with the band 3 to band 2 case leveling off late in the event, while the band 2 to band 2 case continues to drain kinetic energy.

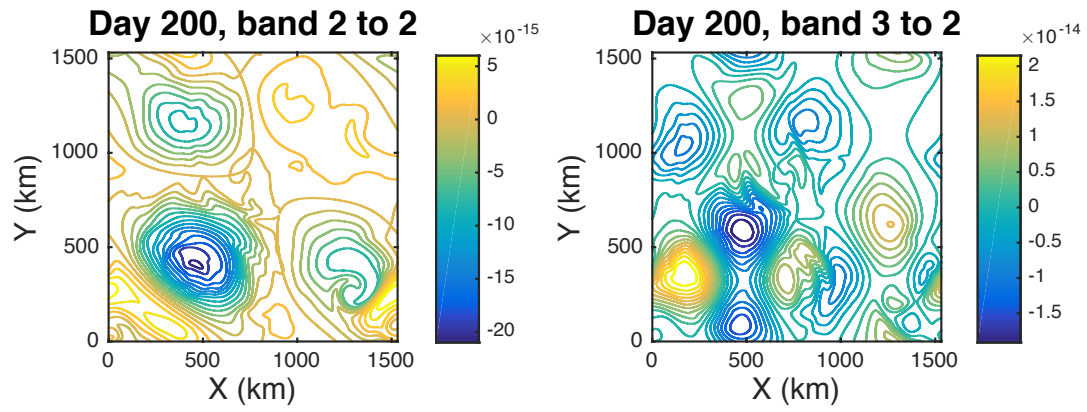


Figure 10: The anatomy of the pressure work occurring at day 200, relatively late in the merger event. The pressure effect on band 2 of band 2 appears on the left and from band 3 to band 2 on the right. The former case is dominated by negative values near regions of cyclones, and reflects the tendencies at these largest scales for cyclones to merge. The distribution on the right hand side is much more evenly distributed between positive and negative values, and indicates a weaker pressure work associated with a more symmetrized, smaller scale structure.

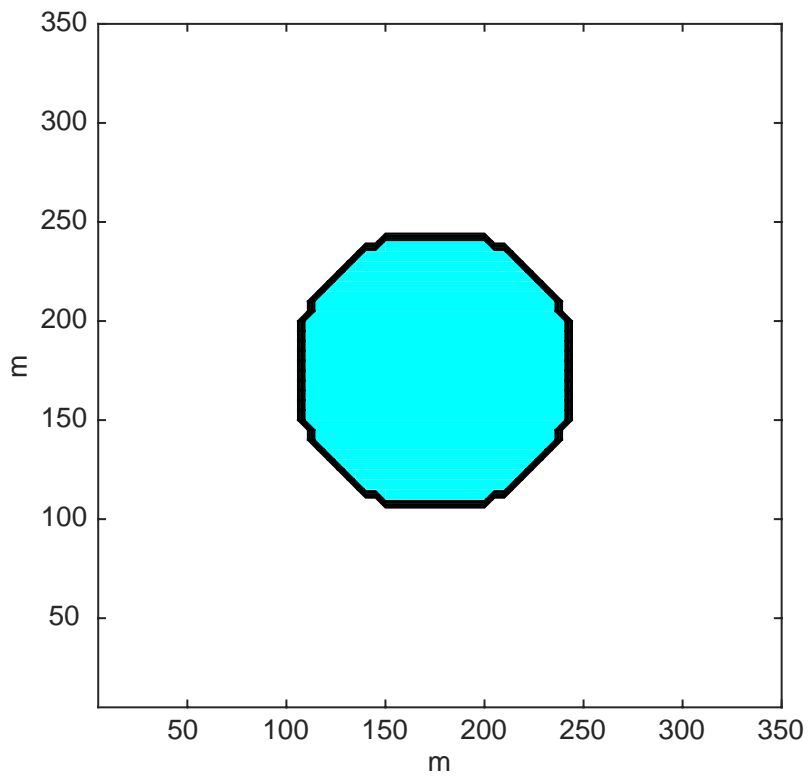


Figure A.11: An example of an irregular domain, consisting of a circular island inside a square domain. The island, outlined in black, occupies about 10% of the area. Vanishing boundary conditions are put on the island boundary and periodic conditions on the outer edge.

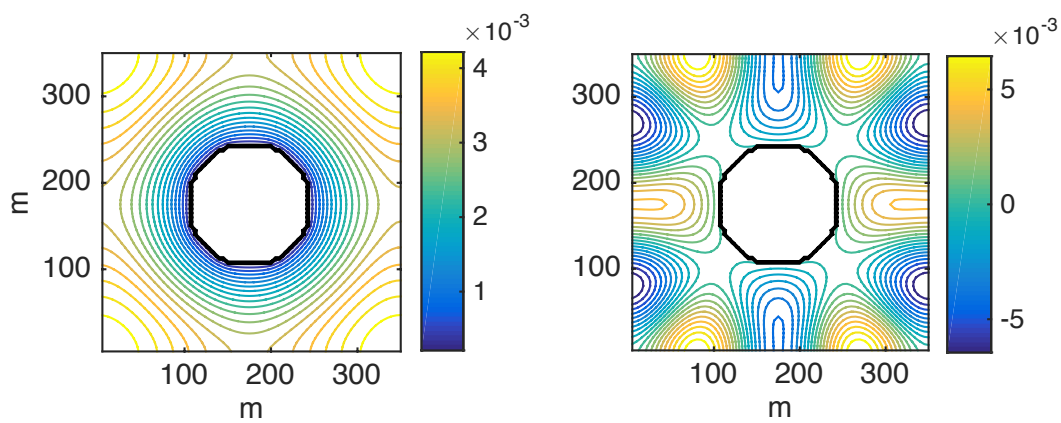


Figure A.12: The first (left) and tenth (right) eigenmodes of the Helmholtz equation for the domain in Fig. A.11. The island location appears in black. Clearly the gravest mode captures the broadest possible scales of the domain and can be associated with the length scale $L = 200m$. The higher mode, however, while more complex spatially, is also measuring comparable length scales of roughly $200m$, in spite of being associated with a much higher eigenvalue.

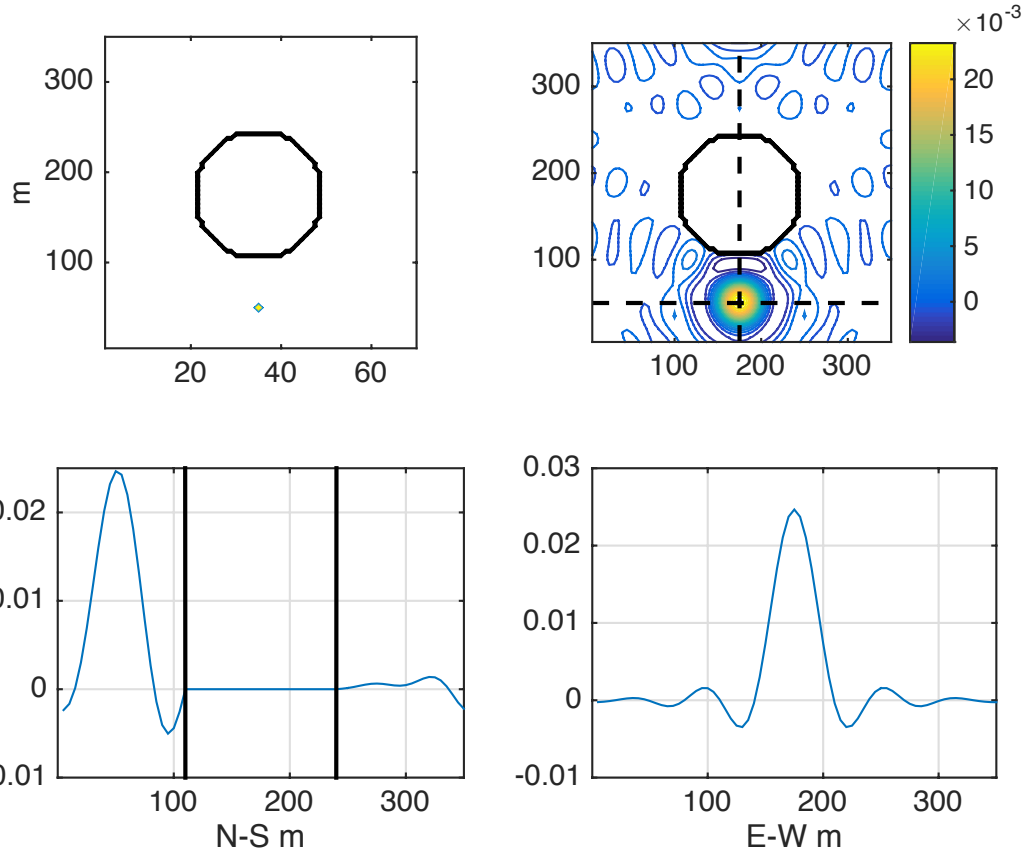
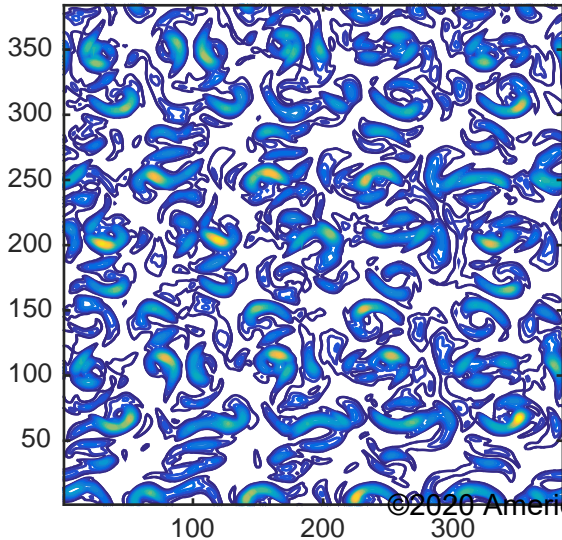


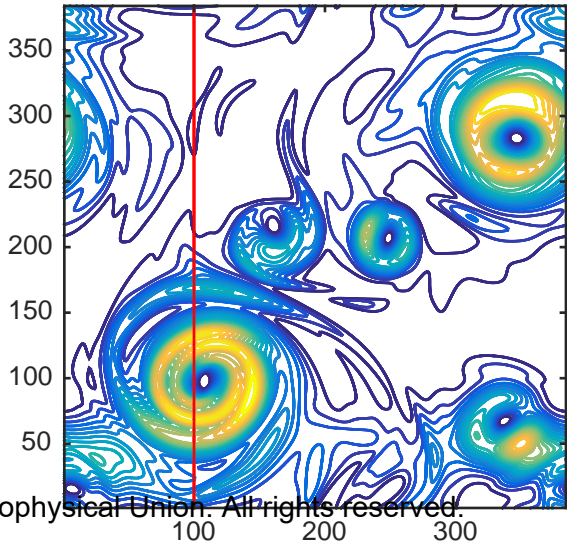
Figure A.13: (top left) The reconstruction of a Dirac delta function inside the domain in Fig. A.11. The island location appears in black (in all panels) and the delta function appears just to the south of mid island. The γ_{100} sampling function (top right). Note that it does not penetrate the island, instead sampling only the active fluid. The dashed black lines denote the locations of the transects appearing in the lower panels. The north-south transect through γ_{100} appears on the lower left. The black lines denote the island location at this longitude. The east-west transect through γ_{100} appears lower right. Note the qualitative resemblance of the structure to a *sinc* function. The distance between neighboring high lobes is roughly 75m and consistent with the rough length scale estimate of 90m associated with the eigenvalue.

Accepted Article

Day 20

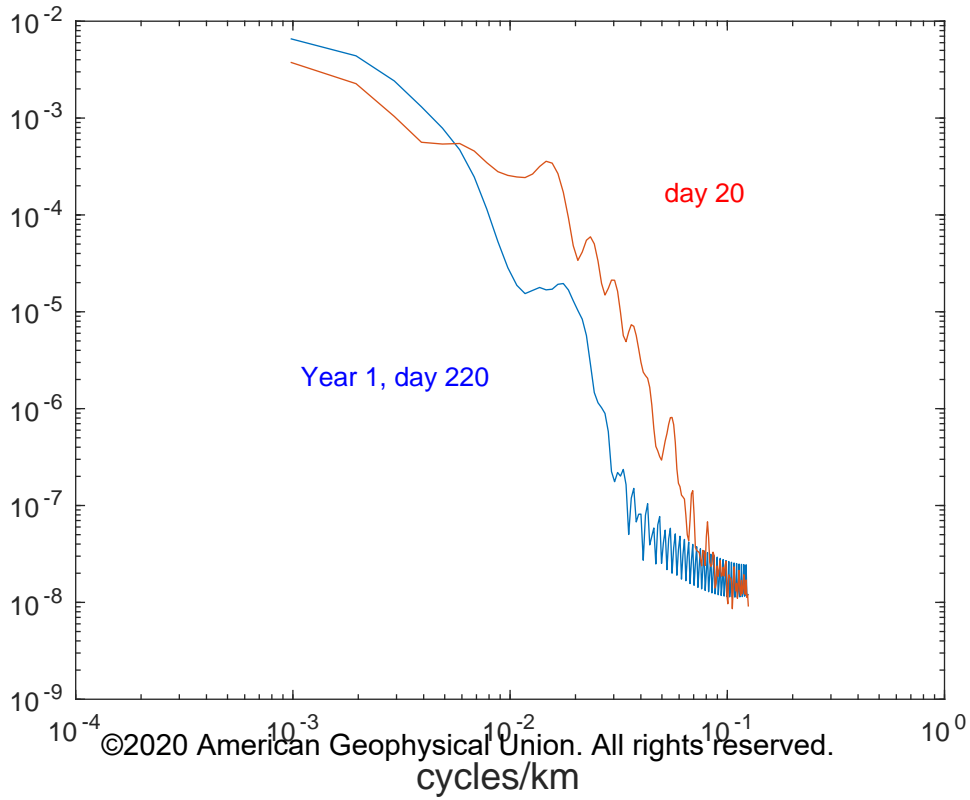


Year 1, Day 220



©2020 American Geophysical Union. All rights reserved.

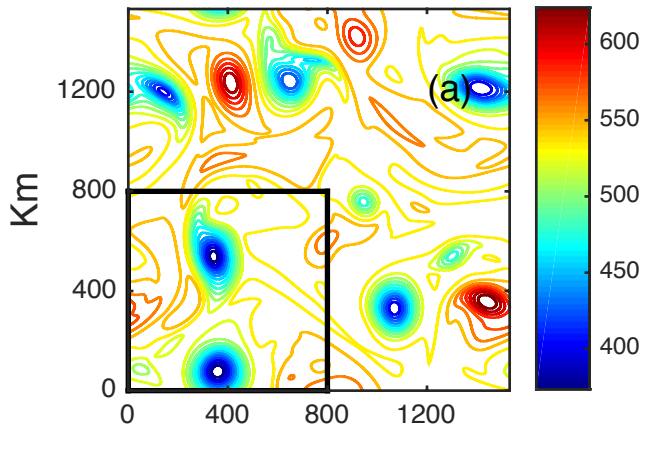
Accepted Article



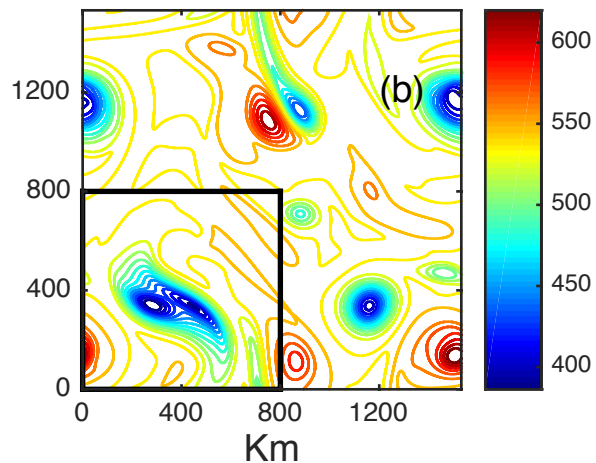
©2020 American Geophysical Union. All rights reserved.
cycles/km

Accepted Article

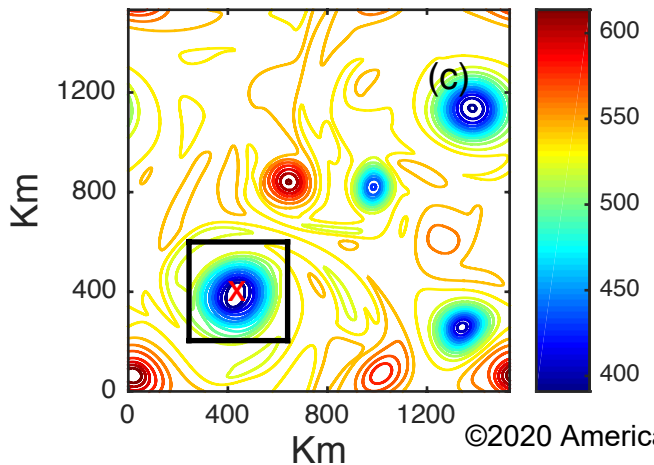
Day 50, Thickness (m)



Day 135, Thickness (m)

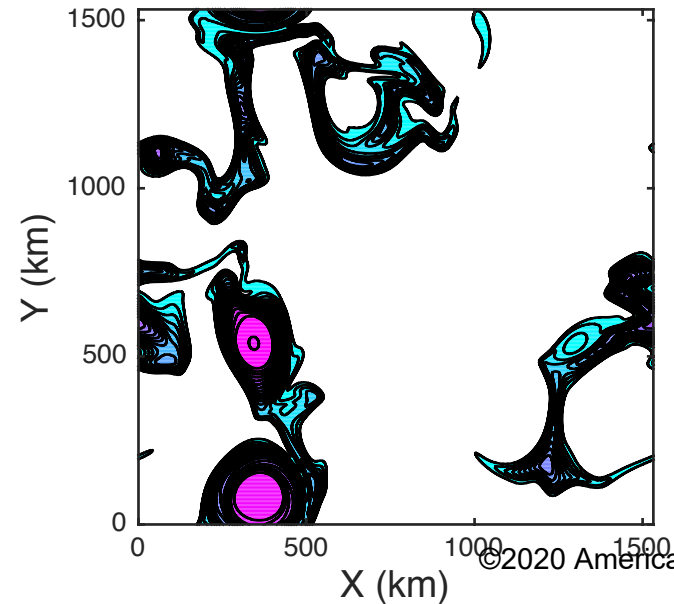


Day 220, Thickness (m)

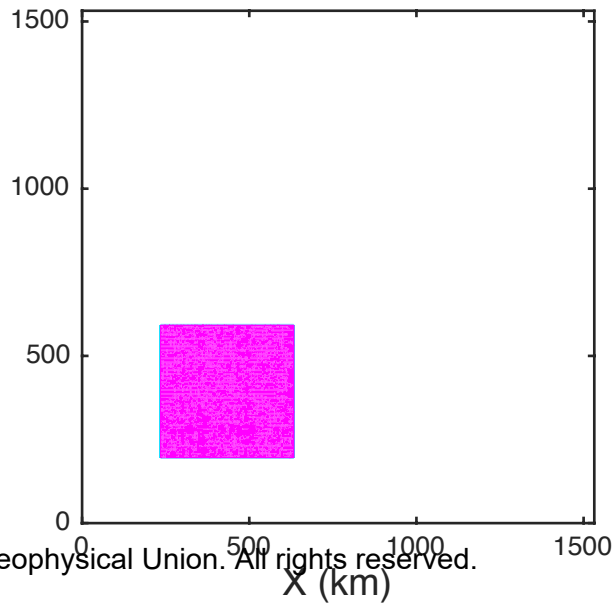


Accepted Article

Day 50 Sample Domain



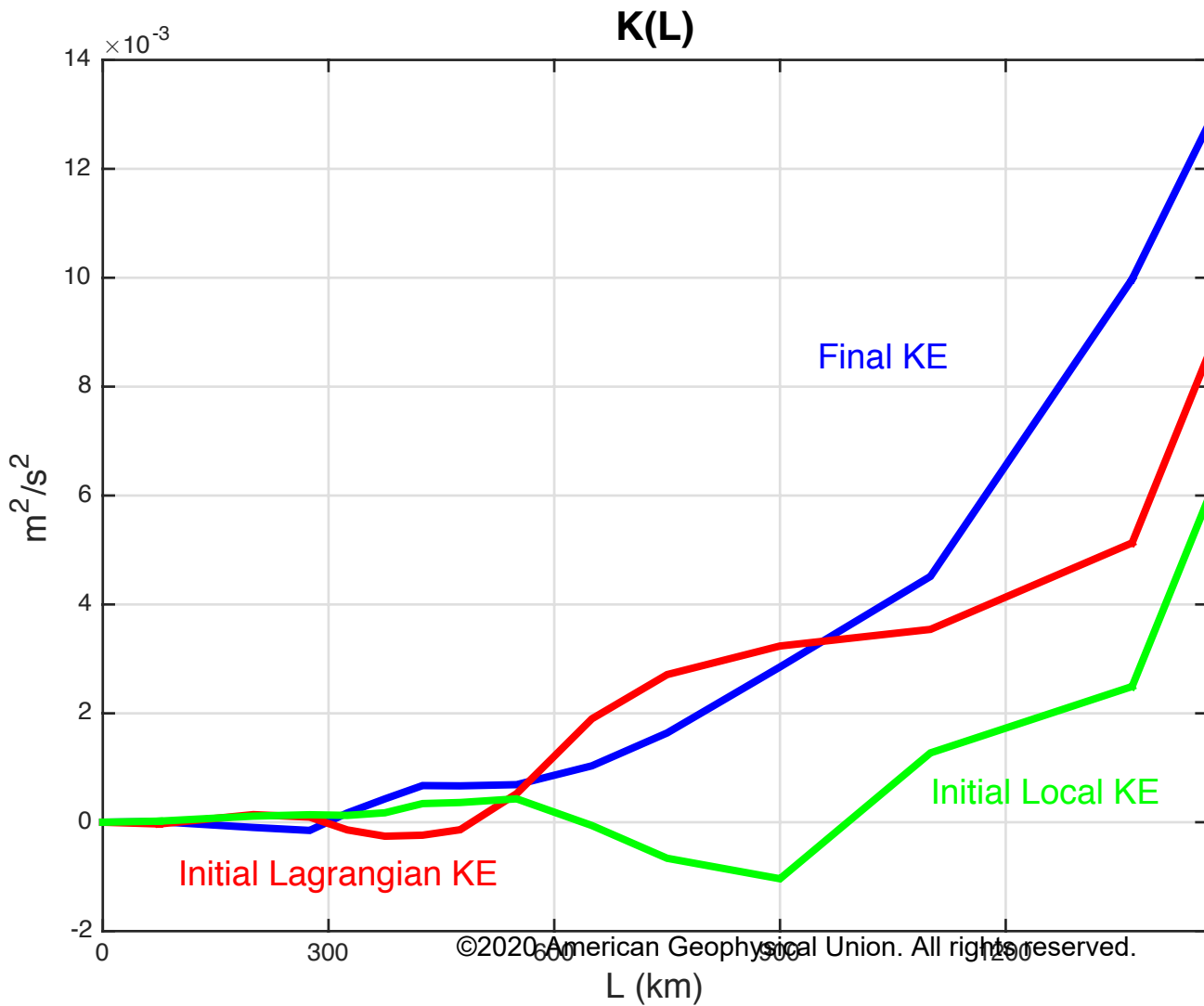
Day 220 Sample Domain



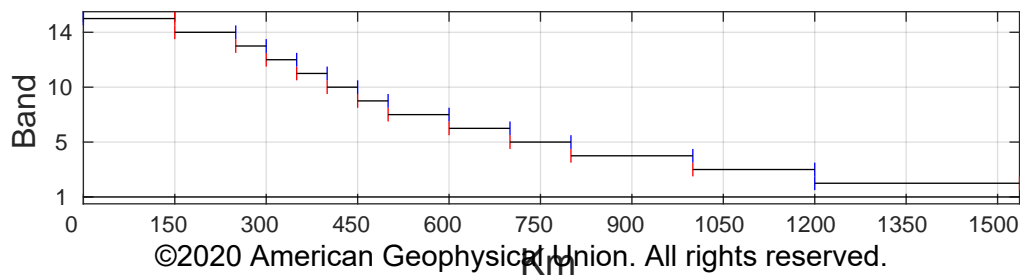
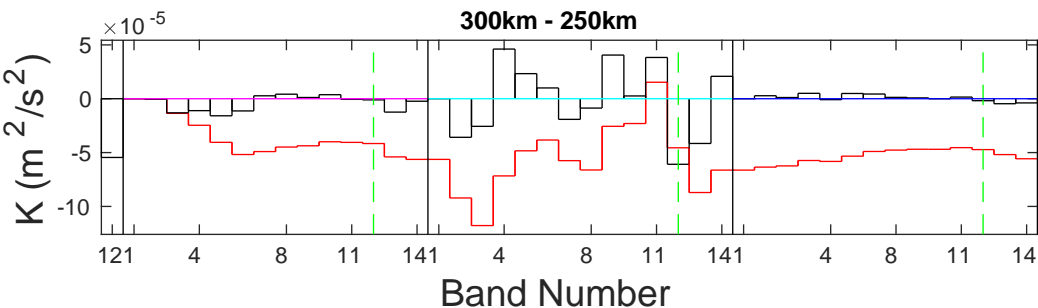
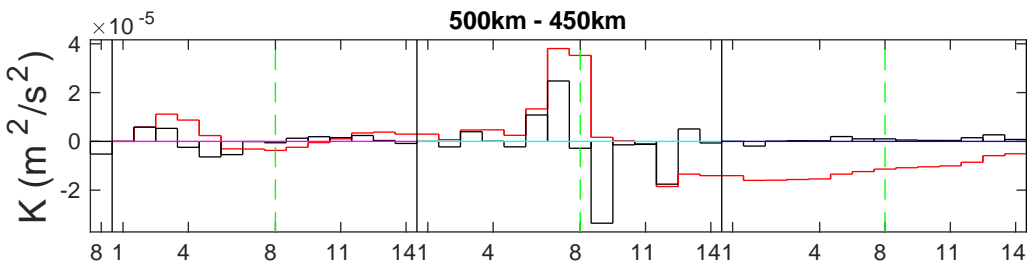
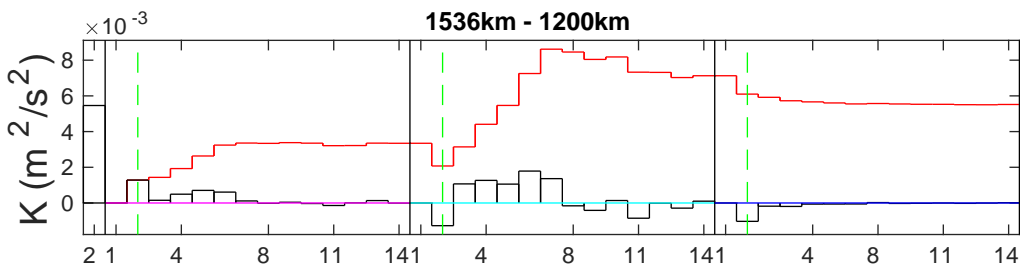
©2020 American Geophysical Union. All rights reserved.

Figure 5.

Accepted Article

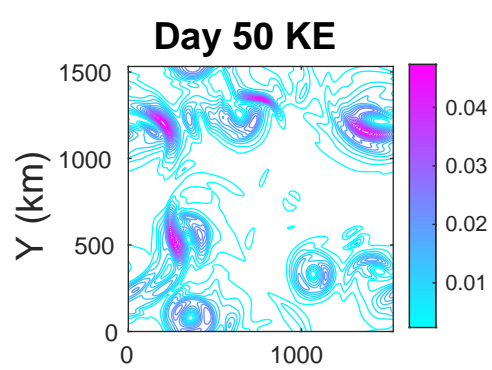


Accepted Article

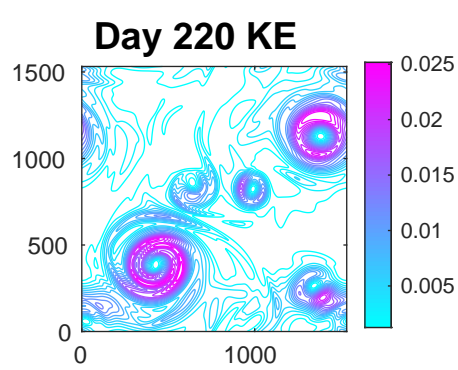


Accepted Article

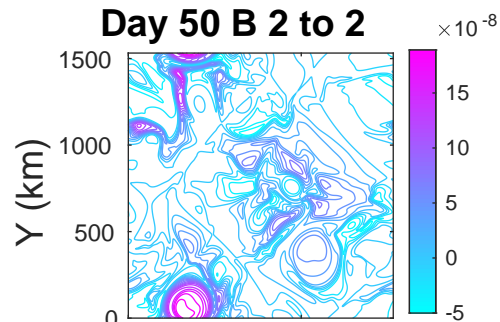
Day 50 KE



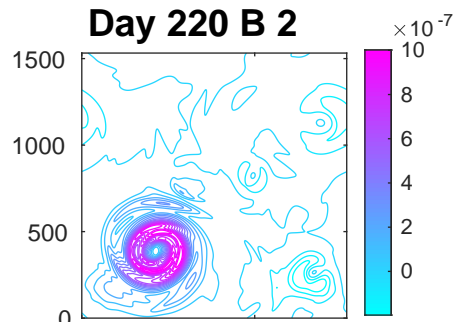
Day 220 KE



Day 50 B 2 to 2

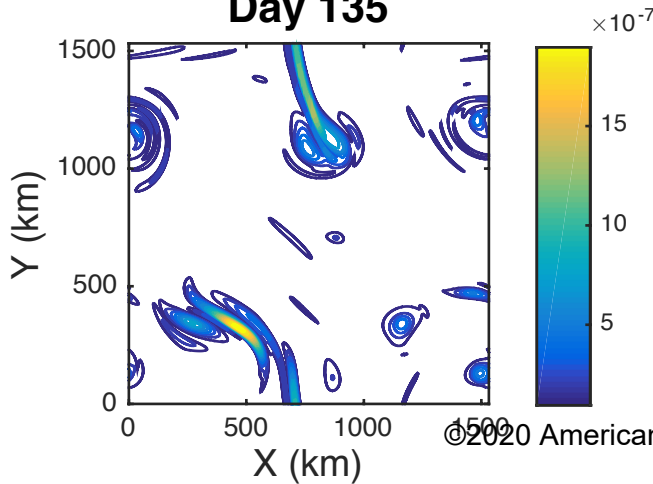


Day 220 B 2

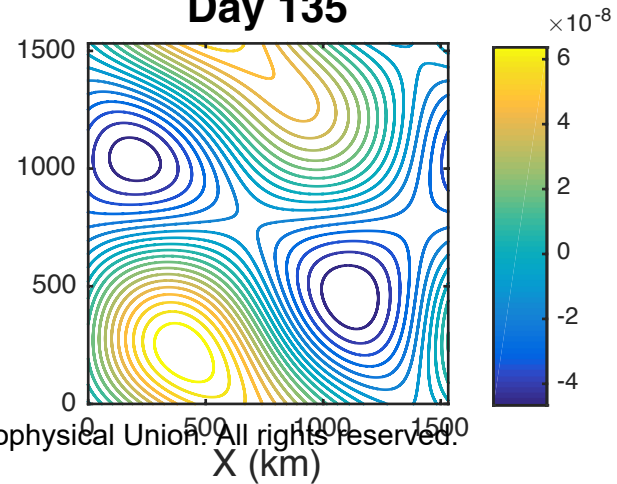


Accepted Article

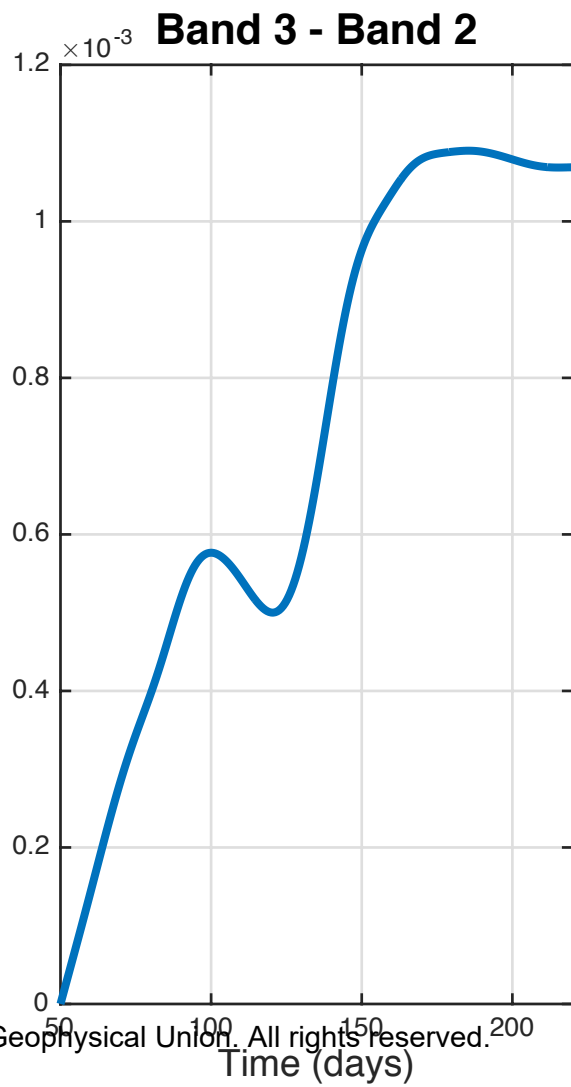
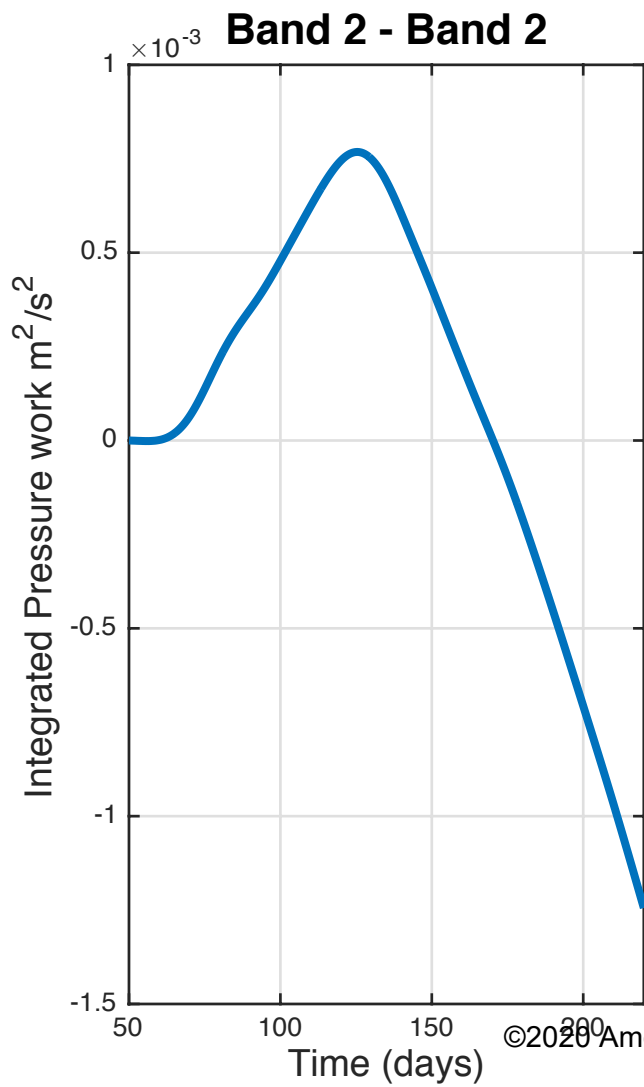
Day 135



Day 135

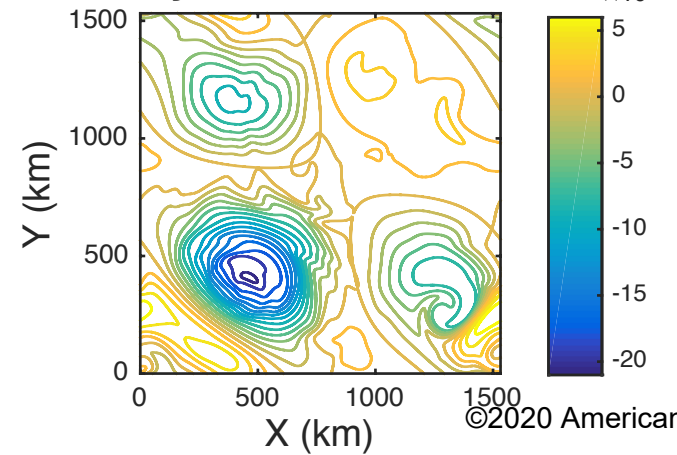


Accepted Article

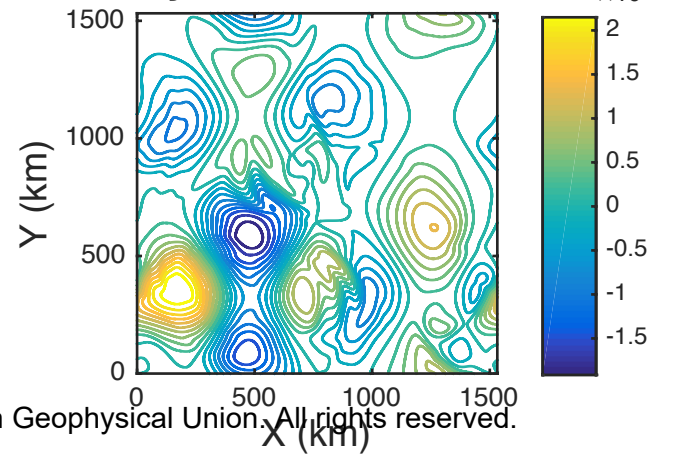


Accepted Article

Day 200, band 2 to 2

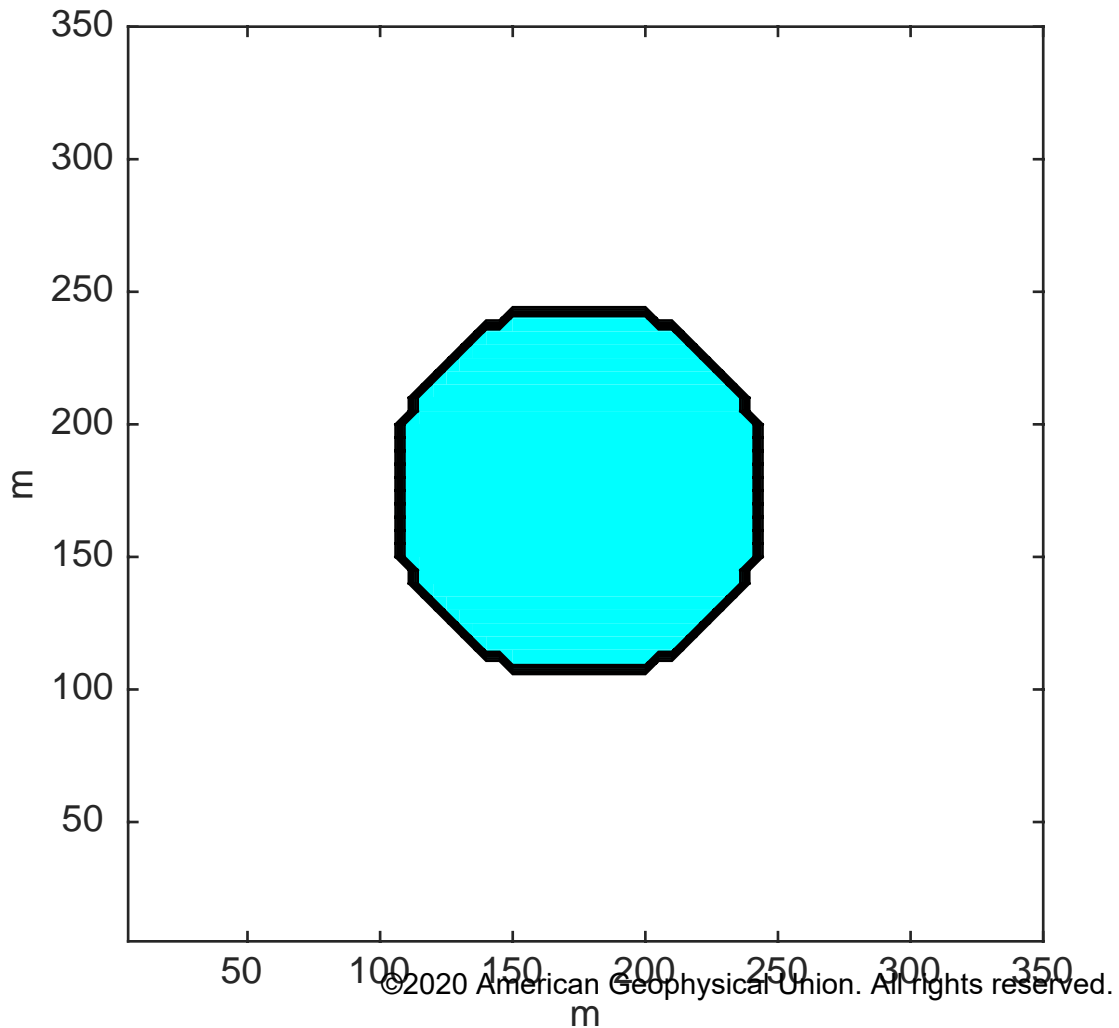


Day 200, band 3 to 2



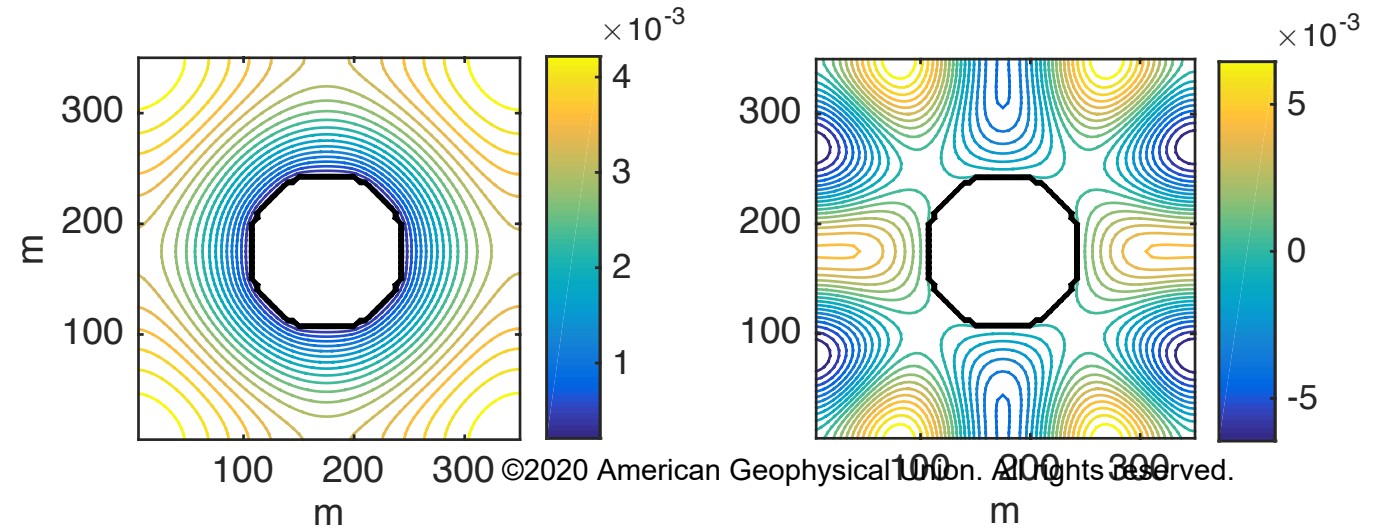
©2020 American Geophysical Union. All rights reserved.

Accepted Article



©2020 American Geophysical Union. All rights reserved.

Accepted Article



Accepted Article

